AGU PUBLICATIONS

Geochemistry, Geophysics, Geosystems

RESEARCH ARTICLE
10.1002/2013GC005194

Key Points:
- There are distinct geochemical signals within a sample and even a dolomite grain
- Five different types of dolomite geochemical features can be summarized
- *In situ* analysis is preferential to investigate diagenetic dolomite geochemistry

Supporting Information:
- Supporting Information

Correspondence to:
P. Guan,
pguanl@pku.edu.cn

Citation:
Zhang, W., P. Guan, X. Jian, F. Feng, and C. Zou (2014), *In situ* geochemistry of Lower Paleozoic dolomites in the northwestern Tarim basin: Implications for the nature, origin, and evolution of diagenetic fluids. *Geochem. Geophys. Geosyst.*, *15*, 2744–2764, doi:10.1002/2013GC005194.

Received 6 DEC 2013
Accepted 16 APR 2014
Accepted article online 21 APR 2014
Published online 10 JUL 2014

In situ geochemistry of Lower Paleozoic dolomites in the northwestern Tarim basin: Implications for the nature, origin, and evolution of diagenetic fluids

Wei Zhang[1,2], Ping Guan[1], Xing Jian[1], Fan Feng[1], and Caineng Zou[2]

[1]Key Laboratory of Orogenic Belts and Crustal Evolution, Ministry of Education, School of Earth and Space Sciences, Peking University, Beijing, China, [2]Research Institute of Petroleum Exploration and Development, PetroChina, Beijing, China

Abstract Lower Paleozoic sedimentary rocks in the northwestern Tarim basin were strongly altered by complicated geofluids, which resulted in the occurrence of various diagenetic minerals (e.g., dolomite). Here, *in situ* major, trace, and rare earth element geochemistry of Lower Ordovician diagenetic dolomite grains as well as petrography were performed to unravel the geochemical features, the nature, and origin of the diagenetic fluids. The results indicate that different geochemical information can be detected within a single sample, even within a single dolomite grain. Five generations of diagenetic dolomite have been identified based on geochemical signatures, resulting from four distinct types of diagenetic fluids: (1) HREE enrichment (PAAS-normalized), low ΣREE, no Eu anomaly, low Mn, Ba, moderate Fe, and high Sr contents are probably due to early burial dolomitizing fluids; (2) MREE enrichment, high ΣREE, high Mn, Fe, and low Sr content are likely to be associated with Devonian deep-circulating crustal hydrothermal fluids; (3) flat or LREE enrichment pattern with obviously positive Eu anomaly is inferred to be linked to Permian magmatic hydrothermal fluids; and (4) flat REE pattern, moderate ΣREE, no Eu anomaly, low Mn, Ba, moderate Fe, and high Sr contents are probably due to late burial dolomitizing fluids. The significances of *in situ* method demonstrated in this study, compared with the whole rock analysis, include not only contamination-free analysis but also unraveling the internal geochemical variation within a single sample or a mineral grain. Thus, for the geochemical study of complicated diagenetic process, *in situ* method should be preferentially considered.

1. Introduction

The Tarim basin is a large cratonic basin in the Central Asia, which mainly consists of the Precambrian basement rocks overlain by Neoproterozoic and Phanerozoic carbonate and siliciclastic rocks. Lower Paleozoic carbonate rocks were significantly influenced by various geofluids in the northwestern Tarim basin [*Jin et al*., 2006; *J. Zhang et al*., 2008; *X. Zhang et al*., 2008a]. Abundant pores, fractures, and vugs as well as diagenetic minerals (e.g., dolomite, calcite, quartz, fluorite, barite, anhydrite, and pyrite) were formed [*Jin et al*., 2006; *Cai et al*., 2008; *Pan et al*., 2009, 2012], resulting in effective reservoirs for hydrocarbons [*Cai et al*., 2008; *Han et al*., 2009; *Pan et al*., 2009; *Li et al*., 2011; *ZHu et al*., 2010; *Jiao et al*., 2011]. Based on drilling well and outcrop samples, three different types of diagenetic fluids were identified by previous studies, including meteoric water, concentrated seawater or heated formation water, and hydrothermal fluid. These studies concluded that the diagenesis of Lower Paleozoic carbonate rocks was controlled by one or the mixture of the above three types of diagenetic fluids [e.g., *Jin et al*., 2006; *Cai et al*., 2008; *Li et al*., 2011; *Zhang et al*., 2011; *Zhu et al*., 2010; *Pan et al*., 2012; *Qian et al*., 2012; *Ji et al*., 2013].

Among the diagenetic minerals, dolomite, which has several different occurrences, is a product of the complicated and multistage dolomitization and diagenesis [e.g., *J. Zhang et al*., 2008; *X. Zhang et al*., 2008a; *Hu et al*., 2010; *Shao et al*., 2010; *Qian et al*., 2012; *Zhao et al*., 2012], but the source and nature of the fluids remains debated. *J. Zhang et al*. [2008], *X. Zhang et al*. [2008a], and *Han et al*. [2009] considered the matrix dolomite and rhombus dolomite filling were precipitated from concentrated basinal seawater or heated basinal water. The saddle dolomite and recrystallized dolomite were precipitated from magmatic hydrothermal fluid [*Chen et al*., 2009; *Pan et al*., 2009; *Zhu et al*., 2010; *Jiao et al*., 2011; *Xing et al*., 2011; *Zhao et al*., 2012; *Dong et al*., 2013a]. However, some studies advocated these dolomites were precipitated from stratigraphic hydrothermal fluid [*Pan et al*., 2012], i.e., the heated formation water [*Qian et al*., 2012] from

Cambrian dolomite strata [*Zhang et al*., 2009], possibly with the involvement of deep-circulating meteoric water [*Zhang et al*., 2011].

Most of the conclusions have been based on dolomite whole rock analysis [e.g., *Li et al*., 2011; *Zhu et al*., 2010]. Actually, some dolomites show distinct features in different grains within one sample, even in different areas of one grain; thus, the whole rock analysis for these kinds of dolomites would obscure important information of different grains or areas where evidence of various and multistage diagenetic processes occurred [*Webb and Kamber*, 2000; *Nothdurft et al*., 2004; *Lapponi et al*., 2013]. Some studies reported isotope measurements using microdrilled representative carbonate samples [*Lonnee and Machel*, 2006; *Katz et al*., 2006; *Bristow et al*., 2011; *Dong et al*., 2013b]. For instance, the oxygen isotope data ($\delta^{18}O_{VPDB} = -8.3$ to $-13.8‰$) of the growth zones of diagenetic saddle dolomite crystals in the Tarim basin suggest a hetero-thermal dolomitizing fluid origin, which was probably linked to the different stages of Permian magmatism emplacement during the Permian in the Tarim basin [*Dong et al*., 2013b]. However, a variety of contaminants, such as terrestrial particulate matter (notably shale), Fe, Mn oxides, and phosphates, could distinctly alter the geochemical data of the chemical sediments in some cases based on whole rock analysis [*Bolhar et al*., 2004; *Nothdurft et al*., 2004; *Bolhar and Van Kranendonk*, 2007; *Alexander et al*., 2008; *Frimmel*, 2009; *Jian et al*., 2013a, 2013b]. *In situ* geochemical analysis is an effective probe into the origin of the diagenetic minerals, which can not only provide more detailed information than the whole rock analysis but also facilitate to unravel the fluid variations indicated within a single grain [*Schwinn and Markl*, 2005; *Kamber and Webb*, 2007; *Piqué et al*., 2008; *Baldwin et al*., 2011]. *Wang et al*. [2009] and *Hu et al*. [2010] reported the REE patterns for discrimination of geofluids based on *in situ* geochemical data of well samples in the central Tarim basin, but the origin of hydrothermal fluid were not clear. Furthermore, the diagenetic fluids affecting the Paleozoic carbonate rocks and siliceous rocks in the northwestern Tarim basin remains unclear.

This study focuses on the different types of Lower Ordovician diagenetic dolomites in carbonate rocks and siliceous rocks in the northwestern Tarim basin and aims to provide *in situ* geochemical data, patterns, and the corresponding interpretations about the nature, origin, and evolution history of diagenetic fluids, combining petrography and major, trace, and rare earth element composition.

2. Geological Setting and Sampling

The Tarim basin is located in the northwest of China (Figure 1) and covers approximately 560,000 km^2 [*Wang et al*., 2009]. It is surrounded by the curved Tianshan Mountain of Paleo-Asian system to the north and curved West Kunlun-Altun Mountains of Tethys system to the south [*Xu et al*., 2011]. The basin is a large cratonic basin that was developed on continental crust basement consisting of Archean and Proterozoic metamorphic rocks from middle Neoproterozoic due to a rifting process related to breakup of Rodinia [*Tuo and Philp*, 2003; *Lu et al*., 2008]. It has a multiple-stage history of tectonic evolution (e.g., the Caledonian, Hercynian, Indosinian, and Himalayan cycles [*Tang*, 1997]) and can be divided into seven principal structural units (Figure 1), comprising three major Uplifts (Tabei, Central, and Southeast) and four Depressions (Kuche, North, Southwest, and Southeast) [*Wang et al*., 1992].

Sedimentary fill consists of Neoproterozoic beach to shallow marine facies siliciclastic rock and carbonates, followed by Cambrian and Ordovician platform facies limestone and dolomite, slope facies limestone and marlstone, and basinal facies mudstone, shale, and marlstone. Silurian to Carboniferous strata consist of marine sandstone and mudstone [*Cai et al*., 2001a, 2001b, 2008; *Li et al*., 2011]. Permian strata are composed of lacustrine sediment and widely distributed volcanic rock, including basalt, rhyolite, diabase intrusions, and granite intrusions [*Yang et al*., 2007; *C. L. Zhang et al*., 2008; *Zhang et al*., 2010; *Tian et al*., 2010]. Mesozoic and Cenozoic sequence consists of terrestrial fluvial sandstone and mudstone [*Cai et al*., 2001a, 2001b, 2008; *Li et al*., 2011].

The study area is located in the northwestern margin of the Tarim basin, assigned to Kalpin Uplift unit, which is formed late in the Cenozoic [*Zhang et al*., 2001]. Dolomites are widely distributed in the Cambrian and Lower Ordovician, which are divided into eight formations (Figure 2a). We investigated several outcrop sections and found that the Penglaiba Formation, at the bottom of Lower Ordovician is mainly composed of open to restricted platform facies limestones and dolomites with several siliceous rock interlayers. It develops more abundant pores, fractures, vugs, and diagenetic dolomite minerals than other formations. Thus, we selected it as our primary study interval, from which a total of 82 fresh diagenetic dolomite

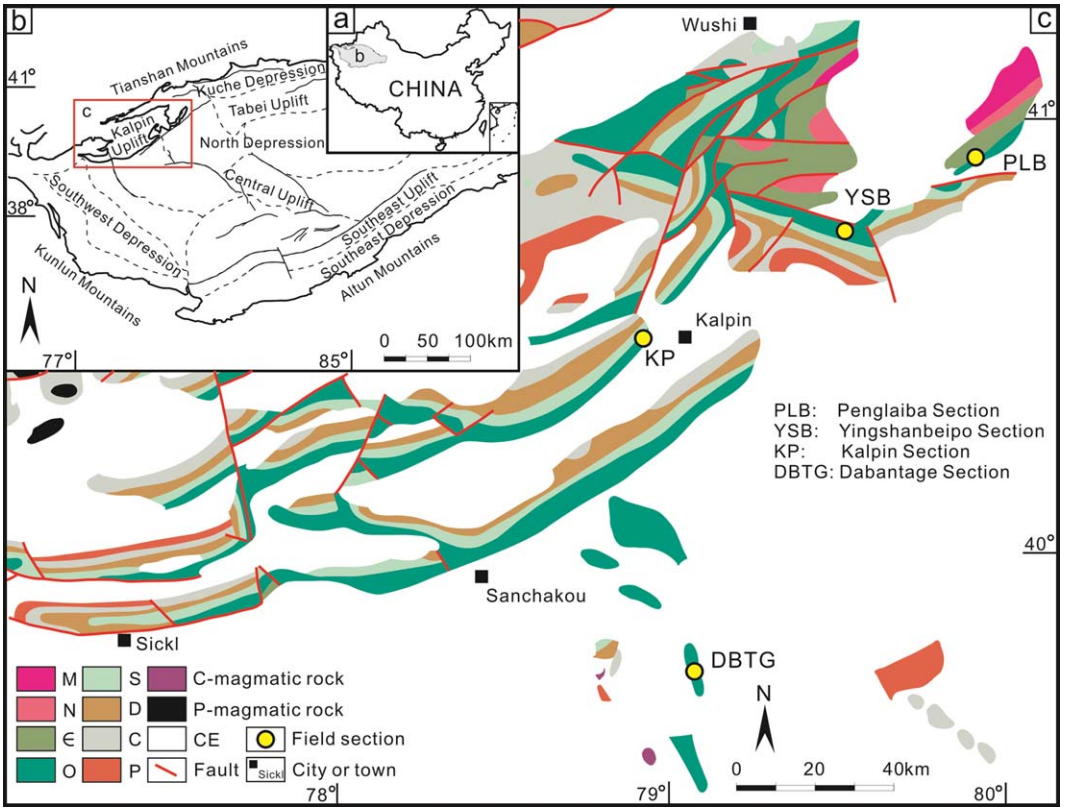

Figure 1. (a) Location of the Tarim basin. (b) Tectonic location of the study area (within the red rectangle) in the Tarim basin. (c) Geological setting of the northwestern Tarim basin and sampling locations. Stratigraphic system: M, Mesoproterozoic metamorphic basement of Aksu Group; N, Neoproterozoic; ∈, Cambrian; O, Ordovician; S, Silurian; D, Devonian; C, Carboniferous; P, Permian; CE, Cenozoic.

samples of different occurrences (minerals filling in fractures and vugs, fluid-altered dolomites, veins, etc.) were collected from four typical outcrop sections (Figures 2b–2e). These four sections can represent regional situation in our study area (Figure 1), i.e., Penglaiba (PLB), Yingshanbeipo (YSB), Kalpin (KP), and Dabantage (DBTG) Sections (Figures 2b–2e).

3. Analytical Procedures

Thin sections were cut from 82 representative samples covering every section and typical occurrence for petrographic observation and cathodoluminescence (CL) analysis. The CL analysis was carried out at the Key Laboratory of Orogenic Belts and Crustal Evolution, Ministry of Education, Peking University, with the conditions of a beam voltage of 5.5 kV and a current of 0.75 mA.

Based on petrographic observation, we classified dolomite types and selected several dolomite mineral grains for each type (a total of 22 grains) as well as different areas in each grain (a total of 170 spots) for *in situ* geochemistry analysis. Major elements (19 grains, 95 spots) were determined by EPMA at MLR Key Laboratory of Metallogeny and Mineral Assessment, Institute of Mineral Resources, Chinese Academy of Geological Sciences, based on the polished, carbon-coated thin sections. A JEOL JXA-8800 electron microprobe was used with the conditions of accelerating voltage of 15 kV, specimen current of 20 nA, and a beam diameter of 5 μm. The detection limits of the microprobe were estimated at approximately 100 ppm.

Trace and rare earth elements (17 grains, 75 spots) were measured by the Laser Ablation Inductively Coupled Plasma Mass Spectrometry (LA-ICP-MS) at the Key Laboratory of Orogenic Belts and Crustal Evolution, Ministry of Education, Peking University. An Agilent 7500ce ICP-MS with the COMPEX Pro102 laser-ablation system equipped with a 193 nm ArF-excimer laser was applied to the trace and rare earth elemental composition measurement [*Li et al*., 2013]. *In situ* LA-ICP-MS analysis has been performed on corals [*Sinclair et al*., 1998], microbial carbonate [*Kamber and Webb*, 2007], larval fish otoliths [*Lazartigues et al*., 2014],

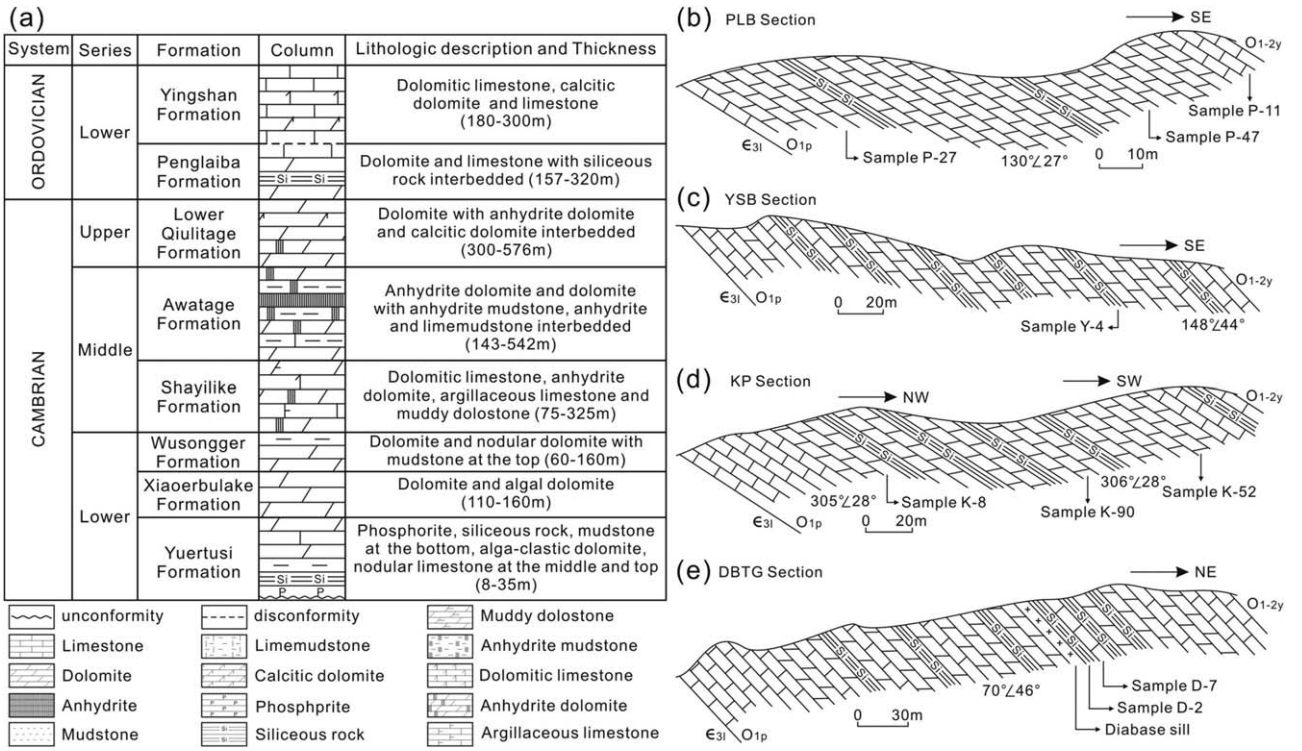

Figure 2. (a) Cambrian-Ordovician stratigraphic framework and lithological description of the northwestern Tarim basin. Draft lithological sections and sample positions for (b) PLB, (c) YSB, (d) KP, and (e) DBTG Sections.

speleothems, and biogenic calcium carbonates [*Jochum et al*., 2012] to study past climate conditions due to its high sensitivity and high spatial resolution. Carbonate reference materials have been tested, and methodology to analyze carbonate samples by LA-ICP-MS was proved to be successful [*Chen et al*., 2011; *Lazartigues et al*., 2014]. The analytical procedure is the same as described by *Gao et al*. [2002]. Helium was used as carrier gas to enhance the transport efficiency of the ablated material. The laser-circular spot sizes were 32, 44, 60, and 90 μm in diameter (note the spot size did not change during the analysis for a single grain) depending on the grain sizes of the analyzed dolomites (Table 1). All measurements were performed using NIST 610 and 612 as external standards and CaO content, determined from EMPA as internal standard. Standards of NIST 610 and 612 were used to monitor analytical quality. The accuracy was estimated to be $<$0.8% for all trace and rare earth elements except Na (2.16%) in NIST 610 and $<$10% except P (28.70%) and Fe (17.76%) in NIST 612 (supporting information Table S1). Detection limits (i.e., background level) were not constant because they were influenced by the beam diameter and equipment conditions [*Lazartigues et al*., 2014]. The detection limits varied from 0.01 to 0.20 ppm for most rare earth elements in this study (supporting information Table S1). Trace element values are normalized to the upper continental crust (UCC) [*Taylor and McLennan*, 1985], and the REE values are normalized to the standard Post-Archean Average Shale (PAAS) [*McLennan*, 1989].

4. Results

4.1. Dolomite Occurrence and Petrology

In the Penglaiba Formation strata, limestones were developed at the bottom and top, dolomites were developed in the middle, and several siliceous rock interlayers were distributed mainly in middle dolomites and also in upper limestones (Figures 2b–2e and 3b). Note that a diabase sill, with the thickness of $\sim$3 m, intruded roughly along the dolomite strata in the DBTG Section (Figures 2e and 3a).

The summary of the petrographic features can be seen in Table 1. Petrographic observation indicates that the dolomite grains have six types as follows: (A) dolomite grains in limestones (Figure 4a); (B) dolomite

AGU Geochemistry, Geophysics, Geosystems

10.1002/2013GC005194

Table 1. An Overview of Locations, Petrology, and Geochemistry for All Samples in This Study[a]

	Location			Petrology				Geochemistry		
Grain No.	Section	Latitude	Longitude	Occurrence	Size (mm)	CL	Type	Mg/Ca	REE	Laser-Circular Spot Size (μm)
P-11-E1	PLB	40°54′51.90″N	79°54′17.90″E	Dolomite grain in limestones	0.20	Nonluminescent	A	Low	T1	32
P-11-E2	PLB	40°54′51.90″N	79°54′17.90″E	Dolomite grain in limestones	0.22	Nonluminescent	A	Low	T1	32
P-11-E3	PLB	40°54′51.90″N	79°54′17.90″E	Dolomite grain in limestones	0.25	Nonluminescent	A	Low	T1	32
K-8-E2	KP	40°33′26.69″N	78°56′25.32″E	Dolomite grain in crystalline dolomites	0.20	Nonluminescent	B	High	T1	60
K-8-E3	KP	40°33′26.69″N	78°56′25.32″E	Dolomite grain in crystalline dolomites	0.20	Nonluminescent	B	High	T1	60
P-27-E3	PLB	40°55′14.72″N	79°55′05.35″E	Dolomite grain in crystalline dolomites	0.45	Nonluminescent	B	Moderate to high	T1	60
P-27-E4	PLB	40°55′14.72″N	79°55′05.35″E	Dolomite grain in crystalline dolomites	0.45	Nonluminescent	B	Moderate to high		60
K-90-E1	KP	40°33′27.90″N	78°56′23.27″E	Rim altered dolomite grain in crystalline dolomites	1.30	Dull red (C)/alternately dull and bright red (R)	B	Moderate to high (R)	T1(C)/T3(R)	44
K-90-E2	KP	40°33′27.90″N	78°56′23.27″E	Dolomite grain in crystalline dolomites	0.60	Nonluminescent	B	High		44
K-90-E3	KP	40°33′27.90″N	78°56′23.27″E	Dolomite grain in crystalline dolomites	0.60	Nonluminescent	B	High		44
P-47	PLB	40°54′59.63″N	79°54′38.94″E	Dolomite grain in crystalline dolomites (C)/saddle dolomite filling in vugs (R)	0.70	Dull red to nonluminescent (C)/bright red (R)	B(C)/C(R)	High (R)	T1(C)/T2(R)	44
K-52	KP	40°33′26.82″N	78°56′15.52″E	Dolomite grain in crystalline dolomites (C)/saddle dolomite filling in vugs (R)	0.60	Dull red to nonluminescent (C)/bright red (R)	B(C)/C(R)	Moderate to high (R)	T1(C)/T2(R)	44
P-27-E1	PLB	40°55′14.72″N	79°55′05.35″E	Saddle dolomite filling in vugs	3.50	Alternately red and nonluminescent along the growth	C	Moderate to high	T2	60
P-27-E2	PLB	40°55′14.72″N	79°55′05.35″E	Saddle dolomite filling in vugs	4.00	Alternately red and nonluminescent along the growth	C		T2	60
D-7-E1	DBTG	39°45′35.60″N	79°02′49.55″E	Dolomite cement in calcarenites	0.30	Nonluminescent	D	High	T3	90
D-7-E2	DBTG	39°45′35.60″N	79°02′49.55″E	Dolomite cement in calcarenites	0.50	Nonluminescent	D	High	T3	90
D-7-E3	DBTG	39°45′35.60″N	79°02′49.55″E	Dolomite cement in calcarenites	0.70	Nonluminescent	D	High		90
D-7-E4	DBTG	39°45′35.60″N	79°02′49.55″E	Dolomite cement in calcarenites	0.80	Nonluminescent	D	High		90
Y-4-E1	YSB	40°44′58.85″N	79°32′11.52″E	Dolomite grain in siliceous rocks	0.40	Dull red (C)/bright red (R)	E	High	T3(C)/T5(R)	90
Y-4-E2	YSB	40°44′58.85″N	79°32′11.52″E	Dolomite grain in siliceous rocks	0.50	Dull red	E		T3	90
D-2	DBTG	39°45′35.60″N	79°02′49.55″E	Dolomite vein in siliceous rocks	0.80	Bright red to orange yellow	F		T3	60
K-8-E1	KP	40°33′26.69″N	78°56′25.32″E	Dolomite vein in siliceous rocks	1.00	Bright red to orange yellow	F	High	T4	60

[a]PLB, Penglaiba Section; YSB, Yingshanbeipo Section; KP, Kalpin Section; DBTG, Dabantage Section; A–F represent dolomite types based on the petrology examination including dolomite grains in limestones, dolomite grains in crystalline dolomites, saddle dolomites filling in vugs, dolomite cements in calcarenites, dolomite grains in siliceous rocks, and dolomite veins in siliceous rocks, respectively; T1–T5 represent five REE distribution patterns (for details see the text); (C), core; (R), rim; blank, the related test was not performed.

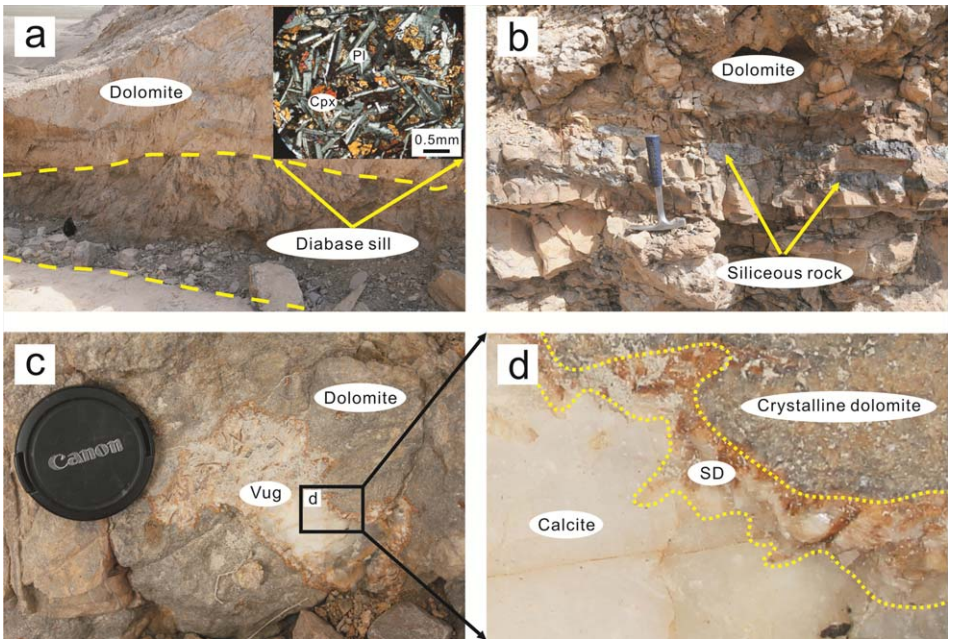

Figure 3. Representative photographs of field sections. (a) An over 3 m thick diabase sill intruded roughly along dolomite strata of the Penglaiba Formation in DBTG Section. Samples D-2 and D-7 are collected at 0.8 and 3.3 m away from the diabase sill, respectively. Pl, Plagioclase; Cpx, Clinopyroxene. (b) Bedded siliceous rocks are common in dolomite strata of the Penglaiba Formation in YSB Section. (c, d) A vug filling with SD (saddle dolomite) and calcite in dolomite strata of the Penglaiba Formation in PLB Section. Note the SD filling in vugs usually distributes between crystalline dolomite and filling calcite.

grains in crystalline dolomites (Figures 4b and 4c); (C) saddle dolomites filling in vugs (Figures 3c, 3d, 4d, and 4e); (D) dolomite cements in calcarenites (Figure 4f); (E) dolomite grains in siliceous rocks (Figure 4g); and (F) dolomite veins in siliceous rocks (Figure 4h). The sketches of these six types of dolomites are illustrated in Figure 4i. The details are described as follows.

Dolomite grains in limestones and crystalline dolomites have nonluminescent CL, while rim-altered dolomite grains in crystalline dolomites (i.e., Sample K-90-E1) shows dull red in the core and alternately dull and bright red in the rim. Saddle dolomite fillings in vugs, which are generally formed between crystalline dolomite and filling calcites, have two distinct subtypes: small grains and large grains. The relatively small grains have dull red to nonluminescent CL in the cores and bright red CL in the rims (i.e., Samples K-52 and P-47), while the larger grains have rims with alternately red color and nonluminescent along the growth (i.e., Samples P-27-E1 and P-27-E2). The heterogeneous dolomite crystals commonly have cloudy cores followed by clear or alternately cloudy and clear rims.

Dolomite grains in siliceous rocks show idiomorphic structure and dull red CL. The rims of the grains show brighter red color than the cores. Furthermore, the diagenetic veins in siliceous rocks are commonly characterized by several stages. For instance, Sample D-2 has diagenetic veins with three stages, i.e., saddle dolomite, quartz, and calcite in order. Sample K-8-E1 has veins with two stages composed by saddle dolomite and quartz (Figure 4h). Therein, the dolomite veins generally show bright red to orange yellow CL.

4.2. Geochemistry

4.2.1. Major Element Composition

The major element composition of the analyzed diagenetic dolomite grains are given in supporting information Table S2.

Theoretical sedimentary dolomites precipitate with the stoichiometric composition (CaO = 30.4%, MgO = 21.7%, Mg/Ca (mol/mol) = 1) [*Warren*, 2000]. While through ongoing dolomitizing diagenesis on sedimentary limestones, Mg^{2+} will substitute Ca^{2+} in crystals and the composition become more stoichiometric along the replacement line. Actually, natural dolomites show lower MgO and CaO, but constant Mg/Ca ratios (shaded area) because other elements will enter lattices (i.e., REEs) [*Chen et al.*, 2010] (Figure 5).

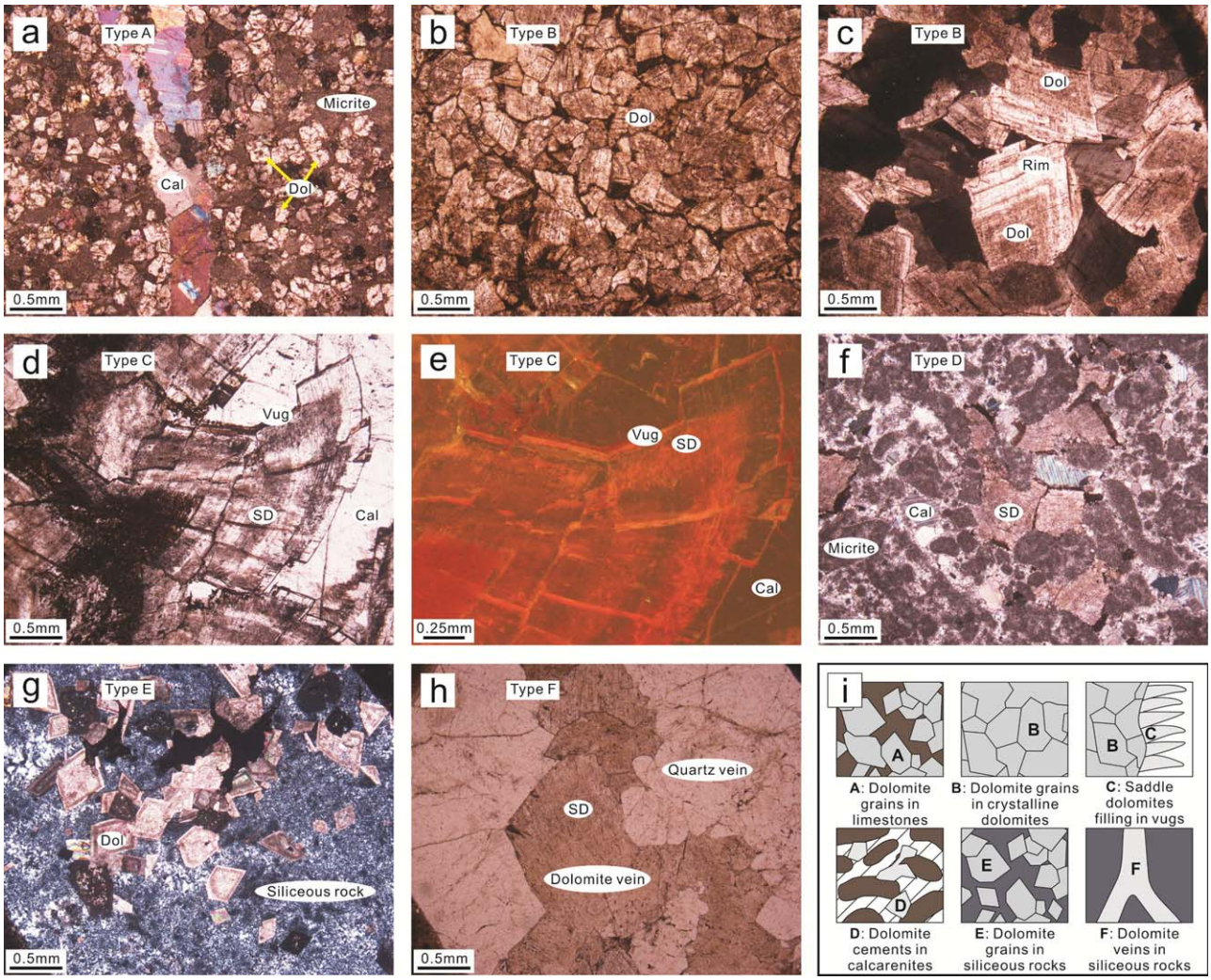

Figure 4. Representative photomicrographs of dolomite samples. (a) Dolomite grains in limestones (Type A, Sample P-11) from PLB Section. (b) Dolomite grains in crystalline dolomites (Type B, Sample P-27-E3) from PLB Section with hypidiomorphic texture. (c) Rim altered dolomite grains in crystalline dolomites (Type B, Sample K-90-E1) from KP Section. (d) Saddle dolomites filling in vugs (Type C, Sample P-27-E1) from PLB Section. (e) CL image of Sample P-27-E1. (f) Dolomite cements in calcarenites (Type D, Sample D-7) from DBTG Section. (g) Dolomite grains in siliceous rocks (Type E, Sample Y-4-E1) from YSB Section. (h) Dolomite veins in siliceous rocks (Type F, Sample K-8-E1), associated with quartz vein from KP Section. (i) Schematic diagram of Types A-F dolomites. Dol, dolomite; Cal, calcite; SD, saddle dolomite.

Types A and B dolomites (e.g., Samples P-11-E1 and K-90-E3) have wide ranges of Mg/Ca ratios (0.80–1.02, av. = 0.90, n = 12). These dolomites predominantly plot in replacement dolomite field (Figure 5) and show positive correlation along the replacement line in the binary diagram between MgO and Mg/Ca [*Chen et al.*, 2010]. Type C dolomites (e.g., Sample P-27-E1) also have wide ranges of Mg/Ca ratios with the range of 0.86–1.03 (av. = 0.97, n = 42, slightly higher than Types A and B dolomites). Note that several analytical spots of Type C dolomites also plot along the replacement line (Figure 5). Most of the Types D, E, and F dolomites (e.g., Sample D-7-E1 and rim of Sample K-90-E1) display high Mg/Ca ratios (0.82–1.02, av. = 0.95, n = 41) and plot near the theoretical composition of stoichiometric dolomite (Figure 5).

4.2.2. Trace and Rare Earth Element Composition

The rare earth and trace element data of the analyzed diagenetic dolomites are given in Table 2 and supporting information Table S3, respectively. Generally, the total REEs abundances (ΣREE) of the dolomites range from 1.61 to 204.8 ppm (av. = 34.40 ppm, n = 75) (Figure 6). The REE distribution patterns are illustrated by normalizing the REEs against PAAS [*McLennan*, 1989] (Figures 7, 8, supporting information Figures S1–S3). Both homogeneous (e.g., Sample P-11-E1) and heterogeneous (e.g., Sample P-27-E1) REE patterns are shown within these analyzed dolomite grains.

Table 2. *In Situ* Rare Earth Element Data of All Samples in This Study[a]

Sample (test spot)	La	Ce	Pr	Nd	Sm	Eu	Gd	Tb	Dy	Ho	Er	Tm	Yb	Lu	∑REE	La_N/Sm_N	Gd_N/Yb_N	Eu/Eu*	Ce/Ce*	Pr/Pr*
P-11-E1.1 (A, T1)	2.16	4.20	0.42	1.84	0.63	0.14		0.07	0.53	0.11	0.15		0.25		10.49	0.50			1.01	0.89
P-11-E1.2 (A, T1)	2.33	4.82	0.67	3.04	0.82	0.11	0.44	0.13	0.37	0.10	0.25		0.53	0.07	13.68	0.41	0.51	0.84	0.89	1.03
P-11-E2 (A, T1)	2.43	4.95	0.56	2.80	0.44	0.15		0.14	0.67	0.16	0.21				12.51	0.80			0.98	0.89
P-11-E3.1 (A, T1)	2.54	4.73	0.54	2.14	0.42	0.10	0.31	0.09		0.14			0.24	0.05	11.29	0.88	0.79	1.25	0.93	1.00
P-11-E3.2 (A, T1)	2.65	4.71	0.52	2.74	0.80	0.14			0.63	0.13	0.22	0.04		0.04	12.62	0.48			0.92	0.86
K-8-E2 (B, T1)	1.15	3.17	0.38	1.45	0.41	0.07	0.30	0.03	0.22	0.06	0.11	0.03	0.17		7.56	0.40	1.05	0.88	1.11	1.03
K-8-E3 (B, T1)	0.86	1.94	0.21	0.69	0.23	0.07	0.14	0.02	0.18	0.05	0.15	0.02			4.57	0.53		1.71	1.05	1.08
P-27-E3 (B, T1)	1.81	3.89	0.42	1.63	0.30	0.08	0.48	0.05	0.35	0.06	0.29	0.03	0.21	0.03	9.62	0.87	1.37	0.93	1.03	0.98
K-90-E1.6 (B, T1)	1.19	2.07	0.14	0.87	0.22				0.14	0.05		0.02	0.08	0.03	4.80	0.78			1.18	0.61
K-90-E1.7 (B, T1)	0.50	0.90	0.12	0.50		0.05				0.03			0.12		2.23				0.85	1.05
K-90-E1.8 (B, T1)	0.38	0.73	0.09		0.28			0.04	0.10						1.61	0.20			0.93	
K-90-E1.9 (B, T1)	0.37	0.64	0.04	0.27	0.23				0.11		0.08				1.74	0.23			1.18	0.60
P-47.7 (B, T1)	1.79	4.15	0.51	2.02	0.27		0.36	0.06	0.35	0.07	0.16	0.03	0.17	0.06	9.98	0.96	1.27		1.00	1.04
P-47.8 (B, T1)	0.45	1.52	0.13	1.14		0.07	0.15	0.07	0.32	0.04	0.26	0.05	0.22		4.42		0.41		1.46	0.58
K-52.2 (B, T1)	2.24	5.66	0.59	2.80	0.68			0.07	0.57		0.30		0.30		13.20	0.48			1.14	0.87
K-52.3 (B, T1)	1.99	4.19	0.38	1.73	0.37			0.06	0.23	0.08	0.26			0.06	9.35	0.78			1.11	0.84
K-52.4 (B, T1)	1.20	2.75	0.37	1.25	0.35	0.11	0.30	0.03	0.24	0.05	0.09	0.04	0.11	0.04	6.92	0.50	1.67	1.54	0.95	1.18
K-52.7 (B, T1)	3.30	7.04	0.75	3.25	0.53		0.36	0.05	0.54	0.12	0.44	0.06	0.23		16.66	0.90	0.97		1.04	0.92
K-52.8 (B, T1)	1.17	2.55	0.25	1.24	0.35		0.40	0.04	0.13	0.05	0.17	0.03			6.37	0.49			1.10	0.81
K-52.9 (B, T1)	1.41	3.09	0.25	1.19	0.35			0.04	0.15	0.05	0.19				6.72	0.59			1.19	0.78
P-27-E1.1 (R1, C, T2)	3.92	12.10	1.75	7.39	1.54	0.53	0.79	0.10	0.77	0.06	0.23	0.04	0.21		29.43	0.37	2.25	2.26	1.07	1.09
P-27-E1.2 (R1, C, T2)	7.28	23.40	3.38	14.39	2.50	0.58	1.32	0.17	0.67	0.14	0.24	0.03	0.31	0.03	54.45	0.42	2.56	1.51	1.09	1.08
P-27-E1.3 (R2, C, T2)	8.77	26.86	3.26	12.89	2.69	0.47	1.93	0.24	1.15	0.21	0.40	0.06	0.26	0.02	59.21	0.47	4.44	0.98	1.16	1.03
P-27-E1.4 (R2, C, T2)	11.86	31.96	3.75	14.91	2.75	0.49	2.12	0.27	1.23	0.21	0.38	0.07	0.25	0.04	70.29	0.63	5.22	0.96	1.11	1.01
P-27-E1.5 (R2, C, T2)	3.53	8.07	0.99	4.14	0.69	0.14	0.59	0.06	0.30	0.05	0.12	0.02			18.70	0.74		1.05	1.00	1.00
P-27-E1.6 (R2, C, T2)	19.11	52.91	6.69	27.28	6.01	1.11	4.52	0.59	2.57	0.47	1.11	0.11	0.62	0.03	123.1	0.46	4.38	1.01	1.08	1.04
P-27-E1.7 (R2, C, T2)	19.90	54.99	7.07	31.73	6.77	1.08	4.89	0.66	2.80	0.50	0.92	0.12	0.46	0.04	131.9	0.43	6.46	0.88	1.07	1.00
P-27-E1.8 (R3, C, T2)	1.61	8.43	2.03	13.87	4.25	0.77	3.96	0.53	2.92	0.48	0.97	0.07	0.73	0.07	40.69	0.05	3.29	0.88	1.08	1.10
P-27-E1.9 (R3, C, T2)	1.20	5.65	1.39	8.72	2.27	0.48	1.76	0.26	1.19	0.22	0.49	0.06	0.17	0.03	23.89	0.08	6.15	1.12	1.01	1.17
P-27-E1.10 (R3, C, T2)	1.82	8.96	1.99	10.99	2.81	0.52	2.38	0.34	1.46	0.26	0.53	0.08	0.39	0.04	32.57	0.09	3.72	0.95	1.09	1.18
P-27-E1.11 (R3, C, T2)	1.41	5.10	1.26	6.43	1.90	0.29	1.58	0.23	1.11	0.18	0.53	0.06	0.26	0.04	20.37	0.11	3.66	0.78	0.88	1.29
P-27-E2.1 (R1, C, T2)	4.34	13.61	1.76	8.54	1.49	0.58	0.91	0.14	0.45	0.07	0.17	0.01			32.07	0.42		2.34	1.14	0.96
P-27-E2.2 (R1, C, T2)	5.76	18.36	2.51	11.28	2.15	0.72	1.39	0.15	0.49	0.09	0.28	0.01	0.10		43.29	0.39	8.10	1.95	1.11	1.02
P-27-E2.3 (R1, C, T2)	6.17	21.31	3.25	13.01	2.78	0.76	1.45	0.15	0.63	0.17	0.26	0.03	0.15	0.02	50.14	0.32	5.99	1.78	1.10	1.15
P-27-E2.4 (R1, C, T2)	6.98	24.76	3.47	14.73	3.41	1.02	1.75	0.22	0.84	0.15	0.37	0.05	0.15	0.03	57.92	0.30	7.16	1.97	1.16	1.07
P-27-E2.5 (R1, C, T2)	3.33	9.09	1.28	5.71	0.94	0.38	0.60	0.10	0.41	0.03	0.15	0.02			22.03	0.51		2.40	1.02	1.05
P-27-E2.6 (R1, C, T2)	2.23	7.30	1.06	5.12	1.33	0.37	1.10	0.13	0.57	0.14	0.35	0.03	0.21	0.03	19.96	0.24	3.21	1.43	1.10	1.02
P-27-E2.7 (R2, C, T2)	10.37	30.29	3.47	14.62	2.97	0.54	2.03	0.25	1.37	0.23	0.41	0.05	0.38	0.04	67.01	0.51	3.27	1.03	1.17	0.97
P-27-E2.8 (R2, C, T2)	19.74	54.62	6.38	24.81	4.87	0.90	3.66	0.43	1.70	0.31	0.62	0.06	0.45	0.02	118.6	0.59	4.98	1.01	1.12	1.02
P-27-E2.9 (R2, C, T2)	29.66	81.00	10.46	42.89	9.15	1.37	5.34	0.76	3.37	0.56	1.05	0.09	0.60	0.07	186.4	0.47	5.37	0.92	1.06	1.04
P-27-E2.10 (R2, C, T2)	21.45	59.22	6.92	27.69	5.23	0.83	3.83	0.45	2.16	0.27	0.83	0.07	0.58	0.07	129.6	0.60	4.01	0.87	1.12	1.01
P-27-E2.11 (R2, C, T2)	20.47	48.10	5.49	22.29	4.13	0.67	2.35	0.29	1.22	0.19	0.38	0.03	0.18		105.8	0.72	7.73	1.02	1.05	0.99
P-27-E2.12 (R2, C, T2)	4.67	12.30	1.66	6.81	1.36	0.27	1.13	0.13	0.73	0.09	0.26	0.02	0.17		29.58	0.50	3.99	1.02	1.02	1.07
P-27-E2.13 (R2, C, T2)	27.07	75.02	9.91	40.08	9.27	1.34	5.50	0.74	3.36	0.58	1.24	0.15	0.74	0.08	175.1	0.42	4.52	0.89	1.06	1.06
P-27-E2.14 (R2, C, T2)	34.05	88.44	11.26	46.67	9.75	1.63	6.16	0.82	3.45	0.53	1.20	0.15	0.62	0.04	204.8	0.51	6.02	0.99	1.04	1.03
P-47.1 (C, T2)	2.71	7.84	1.21	5.37	1.05	0.10	0.63	0.29	0.26				0.23		19.68	0.37	1.68	0.59	1.00	1.09
P-47.2 (C, T2)	5.01	15.79	1.93	8.25	1.78	0.32	1.04	0.13	0.49	0.17	0.35	0.04	0.53	0.07	35.90	0.41	1.20	1.12	1.17	0.99
P-47.3 (C, T2)	5.48	14.28	1.75	6.57	1.28	0.25	0.89	0.11	0.75	0.14	0.34		0.36	0.05	32.24	0.62	1.48	1.12	1.06	1.06
P-47.4 (C, T2)	1.52	6.23	0.93	3.95	0.63	0.11	0.44	0.04	0.34	0.07					14.25	0.35		0.97	1.21	1.10
P-47.5 (C, T2)	1.72	5.71	0.84	3.78	0.38	0.07	0.41	0.05	0.29	0.03	0.09	0.04			13.40	0.67		0.88	1.10	1.06
P-47.6 (C, T2)	2.97	8.38	1.04	4.18	0.63	0.14	0.94	0.09	0.84	0.15	0.16	0.05	0.13		19.70	0.68	4.44	0.86	1.10	1.04
K-52.1 (C, T2)	2.82	7.12	1.01	4.20	0.63	0.16	0.76		0.61	0.12	0.21	0.05			17.68	0.65		1.06	0.97	1.09
K-52.5 (C, T2)	1.58	4.17	0.60	2.26	0.58	0.10	0.38	0.12	0.27	0.07	0.14			0.03	10.30	0.40		1.01	0.99	1.16
K-52.6 (C, T2)	1.52	4.35	0.64	3.03	0.66	0.11	0.46		0.46	0.07				0.02	11.32	0.34		0.92	1.02	1.03
D-7-E1 (D, T3)	0.52	0.89	0.11	0.43	0.05	0.02	0.03	0.01	0.05	0.01	0.02	0.003	0.03	0.003	2.18	1.40	0.63	2.69	0.86	1.05
D-7-E2 (D, T3)	0.45	0.79	0.07	0.39	0.07	0.03	0.09	0.01	0.05	0.01	0.03	0.01		0.01	2.01	1.00		1.56	1.02	0.76
Y-4-E1.2 (E, T3)	1.28	3.02	0.25	1.10	0.28	0.13	0.18	0.03	0.25	0.04	0.15	0.01	0.14	0.01	6.89	0.65	0.79	2.73	1.23	0.82
Y-4-E2.1 (E, T3)	2.95	6.62	0.59	2.24	0.40	0.13	0.36	0.06	0.40	0.07	0.24	0.04	0.28	0.06	14.43	1.08	0.77	1.64	1.16	0.90
Y-4-E2.2 (E, T3)	2.77	4.31	0.39	1.49	0.34	0.10	0.22	0.05	0.18	0.05	0.13	0.01	0.13	0.02	10.19	1.18	1.04	1.73	0.96	0.90
Y-4-E2.3 (E, T3)	2.85	4.98	0.45	1.76	0.36	0.17	0.27	0.03	0.25	0.07	0.17	0.02	0.21	0.03	11.60	1.17	0.79	2.59	1.02	0.89
D-2.1 (F, T3)	2.62	6.80	0.74	2.79	0.58	0.13	0.24	0.04	0.42	0.05	0.10	0.04	0.13	0.02	14.70	0.66	1.16	1.65	1.12	1.00
D-2.2 (F, T3)	1.62	3.83	0.37	1.34	0.34	0.07	0.21	0.05	0.19	0.04	0.13	0.03	0.11		8.32	0.69	1.13	1.30	1.14	0.97
D-2.3 (F, T3)	1.79	4.49	0.49	1.97	0.42	0.08	0.12	0.06	0.18	0.06	0.19	0.02	0.22	0.02	10.10	0.63	0.32	1.79	1.11	0.97
K-90-E1.1 (RB, T3)	1.36	3.38	0.44	1.95	0.46		0.27		0.17		0.17	0.04	0.12	0.02	8.38	0.43	1.37		1.01	1.01
K-90-E1.2 (RB, T3)	1.19	2.92	0.36	1.22	0.65	0.15	0.17	0.07	0.16	0.04	0.16		0.19		7.27	0.27	0.52	2.08	1.03	1.12
K-90-E1.3 (RB, T3)	2.67	5.47	0.65	2.50	0.32	0.10	0.30	0.06	0.27	0.08	0.09	0.02		0.04	12.57	1.21		1.45	0.96	1.03
K-90-E1.4 (RB, T3)	2.08	3.91	0.46	1.41		0.14	0.18	0.05		0.04		0.02	0.21		8.49		0.53		0.93	1.14
K-90-E1.5 (RB, T3)	5.55	10.69	1.04	4.27	0.50	0.21	0.35	0.09	0.29		0.10				23.10	1.63		2.37	1.03	0.90

Table 2. (Continued)

Sample (test spot)	La	Ce	Pr	Nd	Sm	Eu	Gd	Tb	Dy	Ho	Er	Tm	Yb	Lu	∑REE	La_N/Sm_N	Gd_N/Yb_N	Eu/Eu*	Ce/Ce*	Pr/Pr*
K-8-E1.1 (F, T4)	14.40	27.04	2.51	9.19	1.44	0.39	1.01	0.11	0.51	0.10	0.18	0.03	0.09	0.05	57.05	1.45	6.66	1.50	1.04	0.94
K-8-E1.2 (F, T4)	8.67	15.34	1.46	5.62	0.48	0.26	0.37	0.06	0.24	0.05	0.25	0.07	0.16	0.04	33.06	2.64	1.37	2.89	0.99	0.93
K-8-E1.3 (F, T4)	16.84	29.30	2.58	9.51	1.33	0.31	0.79	0.08	0.36	0.09	0.12	0.02	0.18	0.04	61.55	1.84	2.70	1.44	1.03	0.91
K-8-E1.4 (F, T4)	11.75	18.05	1.52	5.62	0.48	0.19	0.38	0.05	0.23	0.06	0.08		0.13	0.03	38.56	3.55	1.77	2.05	0.98	0.89
K-8-E1.5 (F, T4)	6.80	13.57	1.40	5.21	0.77	0.25	0.52	0.10	0.44	0.08	0.24	0.03	0.19	0.04	29.63	1.29	1.63	1.88	1.02	0.98
Y-4-E1.1 (RE, T5)	3.46	7.95	0.74	2.89	0.42	0.12	0.49	0.10	0.57	0.11	0.24	0.04	0.28	0.03	17.44	1.20	1.06	1.21	1.14	0.91
Y-4-E1.3 (RE, T5)	2.53	6.20	0.63	2.61	0.64	0.13	0.49	0.08	0.48	0.08	0.41	0.05	0.32	0.05	14.70	0.57	0.93	1.07	1.13	0.92
Seawater×10^6	0.05	0.00	0.03	0.03	0.04	0.05	0.06	0.06	0.07	0.10	0.11	0.12	0.11	0.12	5.21	1.31	0.57	1.12	0.10	1.48

[a]All values are in ppm. Blank, below detection limits; A–F represent dolomite types based on the petrology examination (for details see the text); RB, rim of dolomite grain in crystalline dolomites; RE, rim of dolomite grain in siliceous rocks; T1–T5 represent dolomite types divided by geochemical features. The data of Post-Archean Average Shale (PAAS) in normalized calculation were from *McLennan* [1989]. Eu, Ce, and Pr anomaly values were calculated by $Eu/Eu^* = Eu_{SN}/(0.67Sm_{SN} + 0.33Tb_{SN})$, $Ce/Ce^* = Ce_{SN}/(0.5La_{SN} + 0.5Pr_{SN})$, and $Pr/Pr^* = Pr_{SN}/(0.5Ce_{SN} + 0.5Nd_{SN})$ [*Bau and Dulski*, 1996]. The average REE compositions of modern seawater (calculated from *Alibo and Nozaki* [1999]) shown in the table were magnified 10^6 times because modern seawaters have extremely low ΣREE.

The results indicate that most of the Types A and B dolomites have homogeneous geochemical features (e.g., Sample K-8-E2) except Sample K-90-E1. ΣREE of the rim of Sample K-90-E1 (av. = 11.96 ppm, n = 5) are significantly higher than that of the core (av. = 2.59 ppm, n = 4; supporting information Figure S1). The rim of Sample K-90-E1 show flat REE patterns with obviously positive Eu anomalies (Eu/Eu* ranging from 1.45 to 2.37), whereas the core shows heavy-REE (HREE) enrichment and pronounced light-REE (LREE) depletion (av. La_{SN}/Sm_{SN} = 0.40; Figure 6a).

Type C dolomites display REEs signatures that vary within single dolomite grains (Figures 7a and 7b), such as Sample P-27-E1, with the ΣREE values varying between 18.71 and 131.9 ppm (av. = 54.97 ppm, n = 11; Figure 6b). This sample has three types of middle-REE (MREE) enriched patterns (Figure 7a): an outer rim (Rim 1, characterized by the positive Eu anomalies); a middle rim (Rim 2, slightly LREE and obvious HREE depletion with no Eu anomaly); an inner rim (Rim 3, pronounced LREE and HREE depletion lacking a positive Eu anomaly or with a slight negative Eu anomaly).

Other Type C dolomites such as Samples P-47 (supporting information Figure S2) and K-52 (supporting information Figure S3) have similar REE pattern features. The rim ΣREE values of Sample P-47 (av. = 22.53 ppm, n = 6) are slightly higher than the core ΣREE values (av. = 7.20 ppm, n = 2). The rim shows MREE enrichment with no Eu anomaly (av. Eu/Eu* = 0.92, n = 6), whereas the core exhibits HREE enrichment and pronounced LREE depletion.

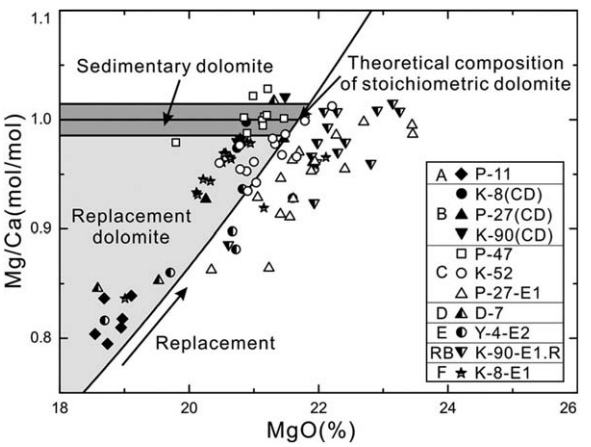

Figure 5. Chemical classification diagram for discriminating replacement dolomites by scatter diagram of Mg/Ca versus MgO after *Warren* [2000] and *Chen et al*. [2010]. For data see supporting information Table S2. A–F represent dolomite types based on the petrology examination (for details see the text); RB, rim of dolomite grain in crystalline dolomites; solid symbol, Types A and B dolomites; open symbol, Type C dolomites; other symbol (half solid), Types D, E, and F dolomites; CD, dolomite grains in crystalline dolomites; R, rim.

Types D, E, and F dolomites generally exhibit homogeneous geochemical characteristics (e.g., Sample D-2) except Sample Y-4-E1 (Type E) (Figure 8). The rim of Sample Y-4-E1 has flat REE patterns without Eu anomaly, while the core displays an obviously positive Eu anomaly (Eu/Eu* = 2.73). Furthermore, the ΣREE of the rim are higher than that of the core, with the average of 16.07 and 6.89 ppm, respectively (Figure 6b).

In summary, the shale-normalized REE distribution patterns of the analyzed diagenetic dolomite grains can be divided into five types: (T1) HREE enrichment, no Eu anomaly, and low ΣREE (e.g., Sample K-8-E2; Figure 9a); (T2) MREE enrichment, various Eu anomalies, and high ΣREE (e.g., Sample P-27-E1; Figures 9b and 9c); (T3) flat REE pattern, positive Eu anomaly, and

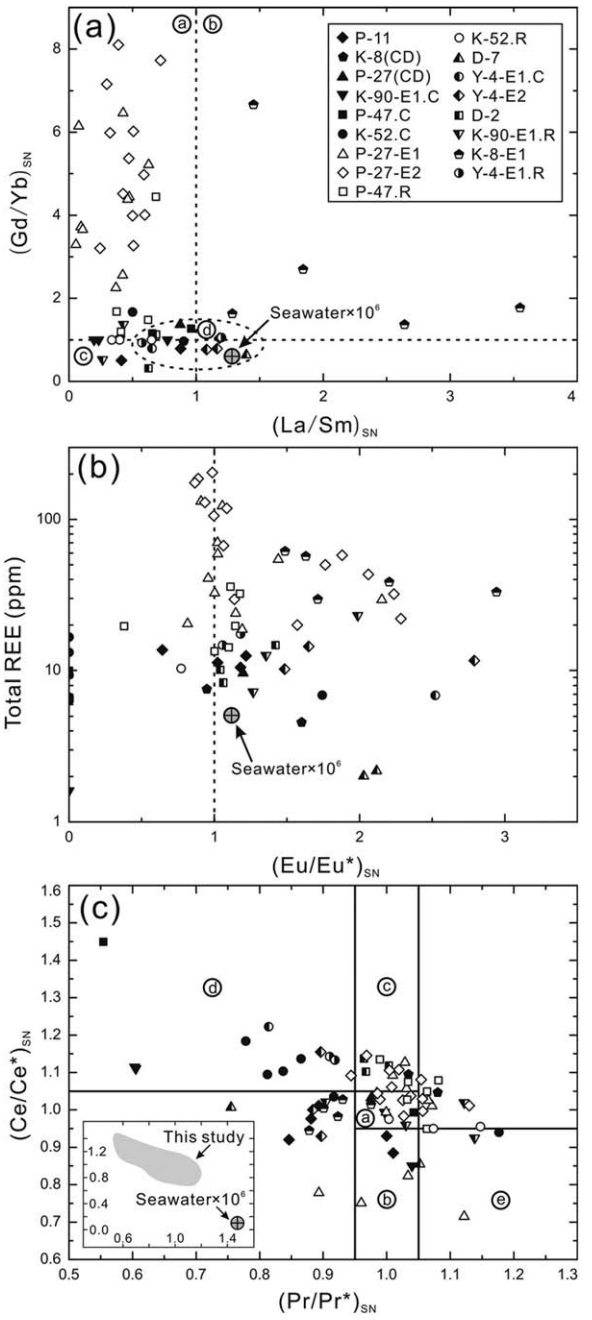

Figure 6. (a) Binary diagram of normalized La/Sm versus Gd/Yb for distinguishing REE distribution patterns. Field a: $(La/Sm)_{SN} < 1$, $(Gd/Yb)_{SN} > 1$, MREE enrichment; Field b: $(La/Sm)_{SN} > 1$, $(Gd/Yb)_{SN} > 1$, LREE enrichment; Field c: $(La/Sm)_{SN} < 1$, $(Gd/Yb)_{SN} < 1$, HREE enrichment; Field d: $(La/Sm)_{SN} \approx 1$, $(Gd/Yb)_{SN} \approx 1$, flat REE pattern. (b) Scatter diagrams of Eu/Eu* versus ΣREE of dolomite samples. (c) Binary diagram showing relationship between Ce/Ce* and Pr/Pr* after *Bau and Dulski* [1996]. Field a, neither Ce nor La anomaly; Field b, positive La anomaly, no Ce anomaly; Field c, negative La anomaly, no Ce anomaly; Field d, true positive Ce anomaly; Field e, true negative Ce anomaly. The average REE compositions of modern seawater (calculated from *Alibo and Nozaki* [1999]) shown in the figures were magnified 10^6 times, because modern seawaters have extremely low ΣREE. Solid symbol, Types A and B dolomites; open symbol, Type C dolomites; other symbol (half solid), Types D, E, and F dolomites; CD, dolomite grains in crystalline dolomites; C, core; R, rim. For data and calculation of Eu/Eu*, Ce/Ce*, and Pr/Pr*, see Table 2 and the text.

moderate ΣREE (e.g., Sample D-2; Figure 9d); (T4) LREE enrichment, positive Eu anomaly, and high ΣREE (e.g., Sample K-8-E1; Figure 9e); and (T5) flat REE pattern, no Eu anomaly, and moderate ΣREE (e.g., rim of Sample Y-4-E1; Figure 9f).

Trace element composition of these diagenetic dolomite samples is normalized to UCC [*Taylor and McLennan*, 1985] and presented in supporting information Figures S4a-S4f. Overall, most samples show relative enrichment of B, V, Mn, and U and relative depletion of Na, Fe, Zn, Sr, Sn, Ba, REEs, and Th, compared to UCC. Note that Ba is enriched in Sample Y-4-E2 and the core of Sample Y-4-E1.

5. Interpretation and Discussion

5.1. Evaluation of Contamination Effects Based on *In Situ* Geochemical Analysis

Previous studies reported that in some cases various contaminants could result in the alteration of whole rock geochemical data of chemical sediments [e.g., *Bolhar et al*., 2004; *Nothdurft et al*., 2004]. For example, incompatible elements (e.g., Al, Ti, Th, Hf, Zr, and Sc), which are commonly concentrated in the detrital minerals [*Goldstein and Jacobsen*, 1988; *Elderfield et al*., 1990], can be enriched as a result of the terrestrial particulate matter contaminants. Thus, a positive correlation is to be expected between ΣREE (relatively high concentration of REE in shale) and these incompatible elements when significant contamination occurs [*Bolhar et al*., 2004; *Bolhar and Van Kranendonk*, 2007; *Alexander et al*., 2008; *Frimmel*, 2009]. In addition, the whole rock data tend to show high transition trace elements (e.g., Cu and Ni) abundances, if Fe, Mn oxides are significant contaminants in carbonate rocks [*Bau et al*., 1996; *Nothdurft et al*., 2004; *Bolhar and Van Kranendonk*, 2007]. Here, the contamination effects are evaluated based on our *in situ* geochemical data of the analyzed dolomites.

The geochemical data of diagenetic dolomite analyzed in this study all have very low Al and Th abundances. The contents

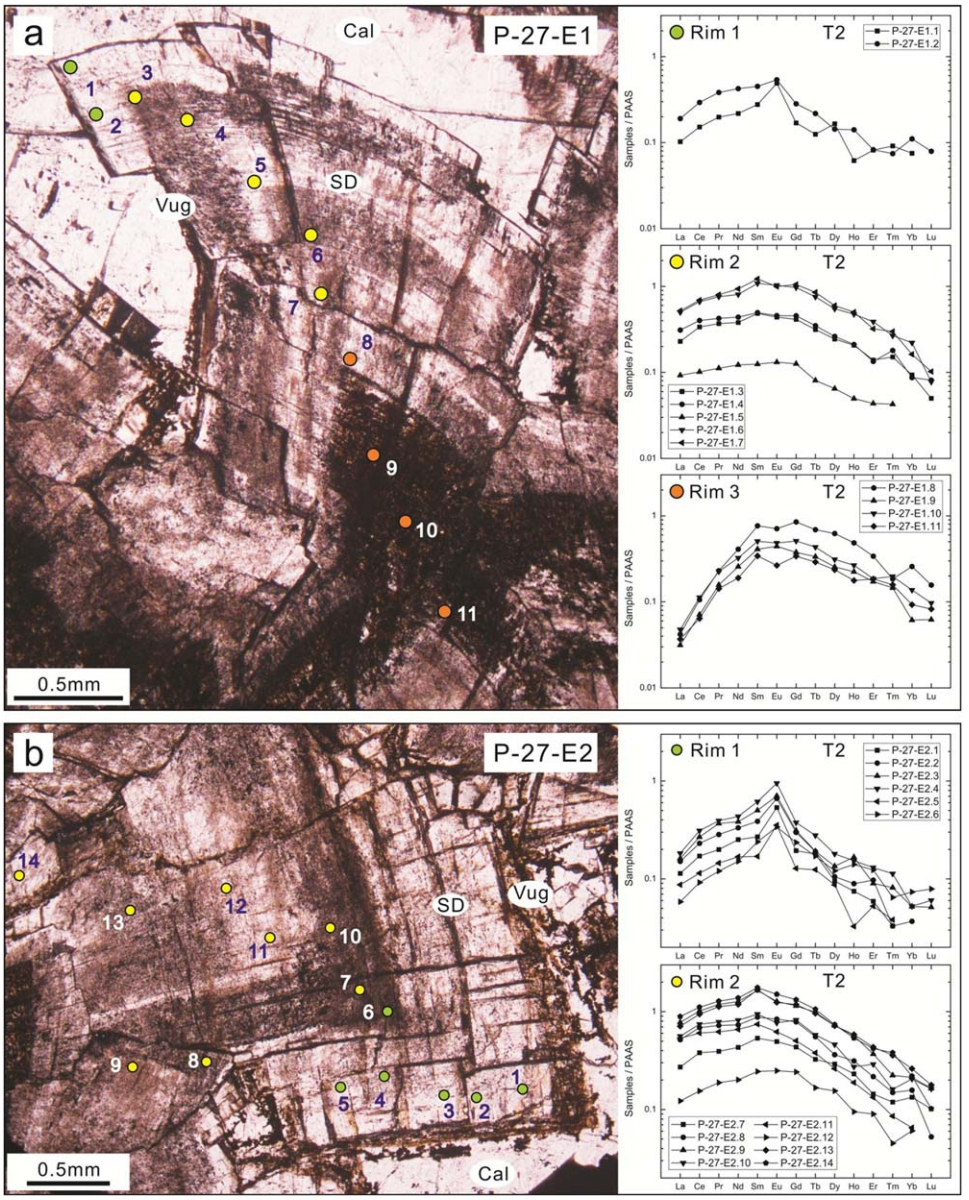

Figure 7. Petrologic and REE features of (a) Sample P-27-E1, (b) Sample P-27-E2. Note the MREE enrichment and slight distinction among inner, middle, and outer rims. The laser-circular spot diameter was 60 μm. SD, saddle dolomite; Cal, calcite; green symbol, Rim 1, outer rim; yellow symbol, Rim 2, middle rim; orange symbol, Rim 3, inner rim.

of Ti, Hf, Zr, Sc, Cu, and Ni of most samples are below the detect limitation. Additionally, there is no correlation between Al, Th, and ΣREE (Figure 10). Hence, all of the data suggest that the dolomite geochemical analysis based on *in situ* method were not influenced by the contamination of terrestrial particulate matter and/or Fe, Mn oxides.

5.2. Comparison to Seawater Geochemical Characteristics

Modern seawater has extremely low ΣREE (with an individual REE ranging from 10^{-6} to 10^{-4} ppm), uniform HREE enrichment, distinctively positive La, slightly positive Gd anomalies, well-documented negative Ce anomaly, and superchondritic Y/Ho ratios [*McLennan*, 1989; *Alibo and Nozaki*, 1999]. The oxidation of Ce^{3+} to Ce^{4+} is the dominant process that leads to negative Ce anomalies in seawater since the Palaeoproterozoic [*Kamber and Webb*, 2001; *Bolhar and Van Kranendonk*, 2007; *Frimmel*, 2009; *Zhao and Jones*, 2013]. Ancient carbonate, which serves as the ancient seawater proxies, indicates that the REE patterns have

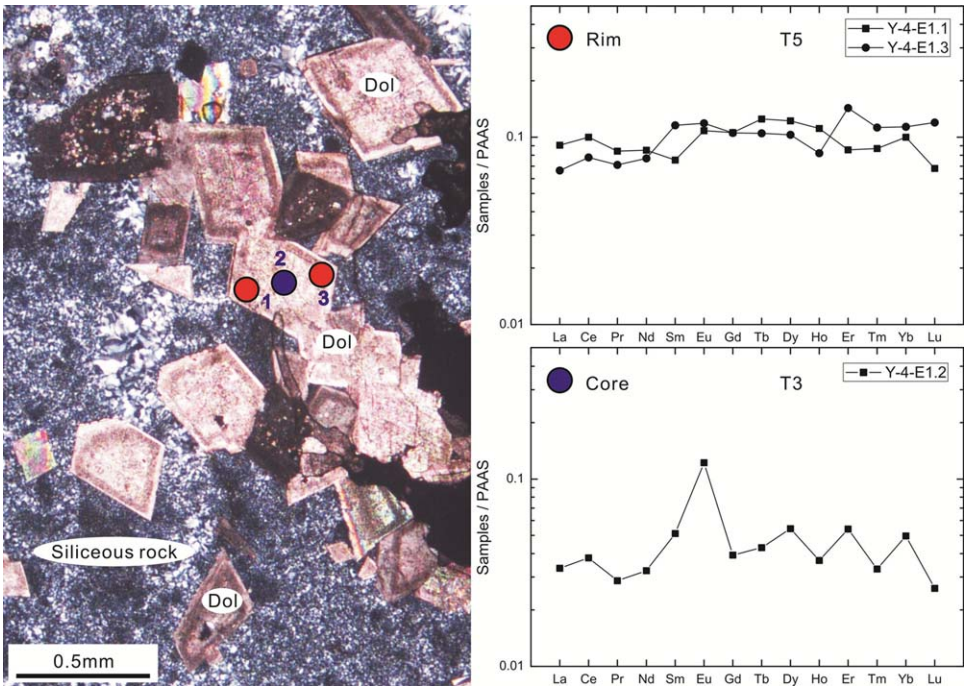

Figure 8. Different petrologic and geochemical features between rim and core of Sample Y-4-E1. Note the positive Eu anomalies in the core and flat REE patterns in the rim. The laser-circular spot diameter was 90 μm. Dol, dolomite; red symbol, rim; blue symbol, core.

remained the same throughout the Phanerozoic [*Webb and Kamber*, 2000; *Shields and Webb*, 2004; *X. Zhang et al*., 2008b; *Zhao and Jones*, 2013].

Our results indicate that most of the analyzed dolomite geochemical data show nonseawater-like features (Figures 6 and 9). Samples with T1 REE patterns also display HREE enrichment, but they do not have a negative Ce anomaly. Therefore, we advocate that the analyzed dolomite crystals were produced from diagenetic fluids rather than the ancient seawater in the northwestern Tarim basin. Furthermore, the differences of REE patterns between dolomite samples and seawater may provide important information about the relative amounts of fluids involved during diagenetic processes [*Tlig and M'Rabet*, 1985; *Banner et al*., 1988; *Qing and Mountjoy*, 1994], from which the degree of the diagenetic alternation can be inferred. Thus, it is inferred that dolomites with T1 REE patterns (e.g., core of Sample P-47; Figure 9a) may be affected least by diagenetic fluids, whereas other dolomites experienced intense diagenesis.

5.3. Geochemical Variations Within Single Dolomite Grain

In this study, 16 dolomite grains show relatively homogeneous elemental compositions, while other six dolomite grains, including Samples K-90-E1, P-27-E1, P-27-E2, P-47, K-52, and Y-4-E1, display geochemical variations within single mineral grain. For example, the cloudy cores of saddle dolomites filling in vugs (Type B, Samples P-47 and K-52) and cloudy core of dolomite grain in crystalline dolomites (Type B, Sample K-90-E1) have T1 REE patterns (HREE enrichment) and dull red to nonluminescent CL, while the clear rims of Samples P-47 and K-52 (Type C) show T2 REE patterns and bright red CL (MREE enrichment) (supporting information Figures S2, S3) and the clear rim of Sample K-90-E1 shows T3 REE patterns and alternately dull and bright red CL (flat REEs and distinct Eu anomaly) (supporting information Figure S1). Likewise, the cloudy core of a dolomite grain in siliceous rocks (Type E, Sample Y-4-E1) has T3 REE patterns and dull red CL, whereas the clear rim has T5 REE patterns (flat REEs and no Eu anomaly) and bright red CL (Figure 8). Furthermore, although Samples P-27-E1 and P-27-E2 (Type C) show the same petrographic features and T2 REE patterns, that is, alternately cloudy and clear features in thin sections, alternately red and nonluminescent CL along the growth, and MREE enrichment with high ΣREE, subtle distinctions in REE features still exist, i.e., the outer rims have obvious positive Eu anomalies (partly similar with T3) (Figure 7).

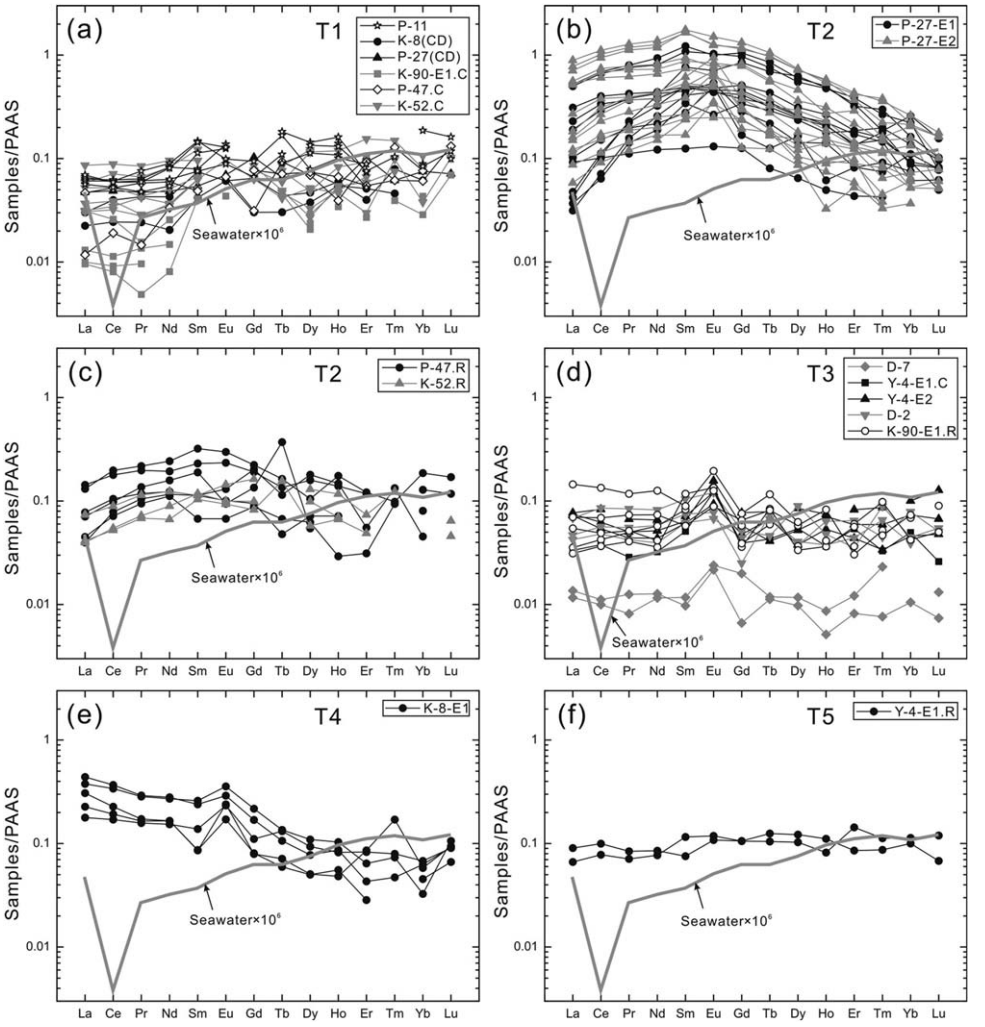

Figure 9. PAAS-normalized REE patterns of dolomites with (a) T1, (b, c) T2, (d) T3, (e) T4, and (f) T5 patterns. The average REE compositions of modern seawater (calculated from *Alibo and Nozaki* [1999]) were magnified 10^6 times. The data of PAAS are from *McLennan* [1989]. CD, dolomite grains in crystalline dolomites; C, core; R, rim. For data see Table 2.

Therefore, according to the geochemical variations within single dolomite grains, dolomites with different geochemical features can be divided into different stages and assigned relative ages, i.e., dolomites with T1 REE patterns were formed earlier than dolomites with T2 and T3 REE patterns, while dolomites with T3 REE patterns should be formed earlier than dolomites with T5 REE patterns.

5.4. Nature and Origin of the Diagenetic Fluids

Here, we discuss the nature and origin of the related diagenetic fluids based on the geochemical data and petrographic observations of the analyzed diagenetic dolomite samples in the northwestern Tarim basin. Several special elements and ratios could serve as the indicators of the formation conditions of the dolomites. For example, Ce^{4+}/Ce^{3+} and Eu^{3+}/Eu^{2+} are controlled by oxidation [*Kamber and Webb*, 2001; *Bolhar and Van Kranendonk*, 2007; *Frimmel*, 2009; *Zhao and Jones*, 2013] and temperature [*Frimmel*, 2009]; thus, the Ce and Eu anomalies can be used to evaluate the oxidation condition of the water and hydrothermal precipitates; high Ba and Mn contents can indicate origin of hydrothermal fluids [*Middleton et al*., 1993; *Chen et al*., 2009]; and the redox-sensitive metallic elements Fe and Mn are prone to be enriched in an oxidative setting [*Morford and Emerson*, 1999].

5.4.1. Dolomite With T1 REE Pattern

Dolomite samples with T1 REE patterns (e.g., Sample P-11-E1) have relatively homogeneous internal structure and geochemical properties, implying relatively stable conditions during formation. These dolomites show

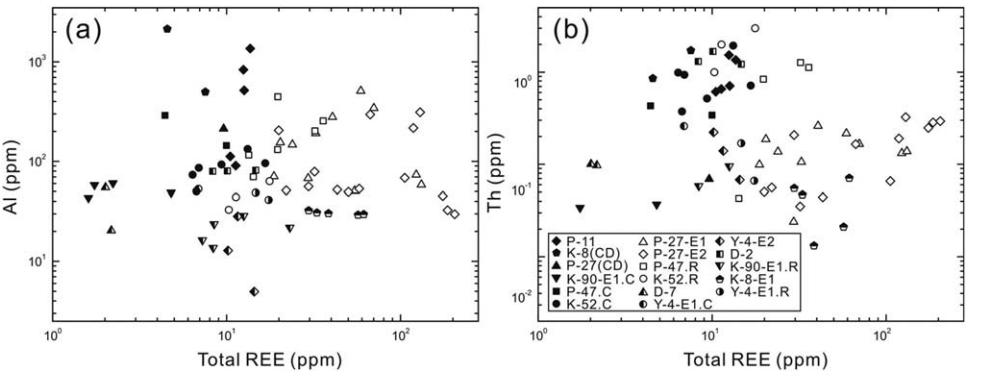

Figure 10. Binary diagrams of (a) Al and (b) Th versus ΣREE for evaluating contamination and alteration of dolomite samples. Solid symbol, dolomites with T1 patterns; open symbol, dolomites with T2 patterns; half left symbol, dolomites with T3 patterns; half up symbol, dolomites with T4 patterns; half right symbol, dolomites with T5 patterns. CD, dolomite grains in crystalline dolomites; C, core; R, rim. For data see Table 2 and supporting information Table S3.

HREE enrichment and slightly positive Ce anomalies or no Ce anomaly (Figures 6a and 6c), different from seawater or precursor carbonates [e.g., *X. Zhang et al*., 2008b; *Zhao and Jones*, 2013]. According to the Ce/Ce* values, moderate Fe, low Ba, and Mn abundances (Figure 11), it is concluded that these dolomites can be linked with the diagenetic fluids of weak oxidation and nonhydrothermal conditions. Previous studies reported that the formation temperature of this kind of dolomites may be lower than 50°C in most cases [*Gregg and Sibley*, 1984; *Shukla*, 1986]. Low Mn abundance also implies that meteoric waters and deep fluids did not influence the dolomites since they should result in high-Mn dolomites [*Jin et al*., 2006]. Furthermore, it is inferred that these dolomites were formed in the early diagenetic stage and scarcely experienced replacement and recrystallization indicated by MgO-Mg/Ca (Figure 5) and Sr-Mn diagrams (Figure 11c) [*Qing*, 1998; *Hecht et al*., 1999; *Jacobsen and Kaufman*, 1999; *Warren*, 2000; *Chen et al*., 2010; *Derry*, 2010].

Based on the above discussion, we contend that diagenesis occurred during shallow burial. Dolomitizing fluids were derived from residual concentrated basinal seawater in the pores under weak oxidation conditions in the early diagenetic stage.

5.4.2. Dolomite With T2 REE Pattern

Dolomite samples with T2 REE patterns (e.g., Sample P-27-E1) probably originated from nonmagmatic hydrothermal fluids. This can be explained as follows. First, T2 REE pattern is characterized by significant MREE enrichment, a so-called roof-shaped (upward convex) REE pattern, which is common for hydrothermal carbonates formed by low-*p*H crustal fluids [*Hecht et al*., 1999]. The LREE depletion is caused by the hydrothermal recrystallization or remobilization of dolomites [*Kučera et al*., 2009], and the HREEs are bound to less soluble minerals additionally causing HREE depletion in diagenetic fluids during REE mobilization [*Morgan and Wandless*, 1980; *Bau and Möller*, 1992; *Lüders et al*., 1993]. Second, these dolomites show high ΣREE (up to 204.8 ppm) and high Mn contents (Figures 6b and 11a), which also are the evidences of occurrence of hydrothermal fluids. Third, the previous study reported that this kind of dolomites in the northwestern Tarim basin had the fluid inclusion homogenization temperatures ranging from 90 to 130°C, mainly ~110°C [*Zhang et al*., 2011], higher than the maximum burial temperature (~100°C) [*Ye*, 1994; *Li et al*., 2005; *Li et al*., 2011; *Zhang et al*., 2011]. However, most of the REE distribution patterns of these dolomite samples show no Eu anomaly (Figure 6b), which suggest that they precipitate at relatively low (or not so high) temperatures (90–130°C), because the positive Eu anomaly is considered to occur at high temperatures (>200–250°C) [*Derry and Jacobsen*, 1990; *Bau*, 1991; *Bau and Dulski*, 1996; *Kučera et al*., 2009; *Azomani et al*., 2013].

Furthermore, dolomite samples with T2 REE patterns plot along the replacement line and near the theoretical composition of stoichiometric dolomite in MgO-Mg/Ca diagram (Figure 5), suggesting sufficient crystallization, which is also supported by relatively high Mn and low Sr contents (Figure 11c). Additionally, these dolomite samples have high Fe abundances (Figure 11b) and slightly negative Ce anomalies or no Ce anomaly (Figure 6c), indicating a suboxic fluid conditions. Lower Ordovician dolomites in eastern Laurentia, which also displayed roof-shaped REE patterns, show similarities with the dolomites of this study and are considered to have formed from high salinity nonmagmatic fluids under suboxic conditions [*Azomani et al*., 2013].

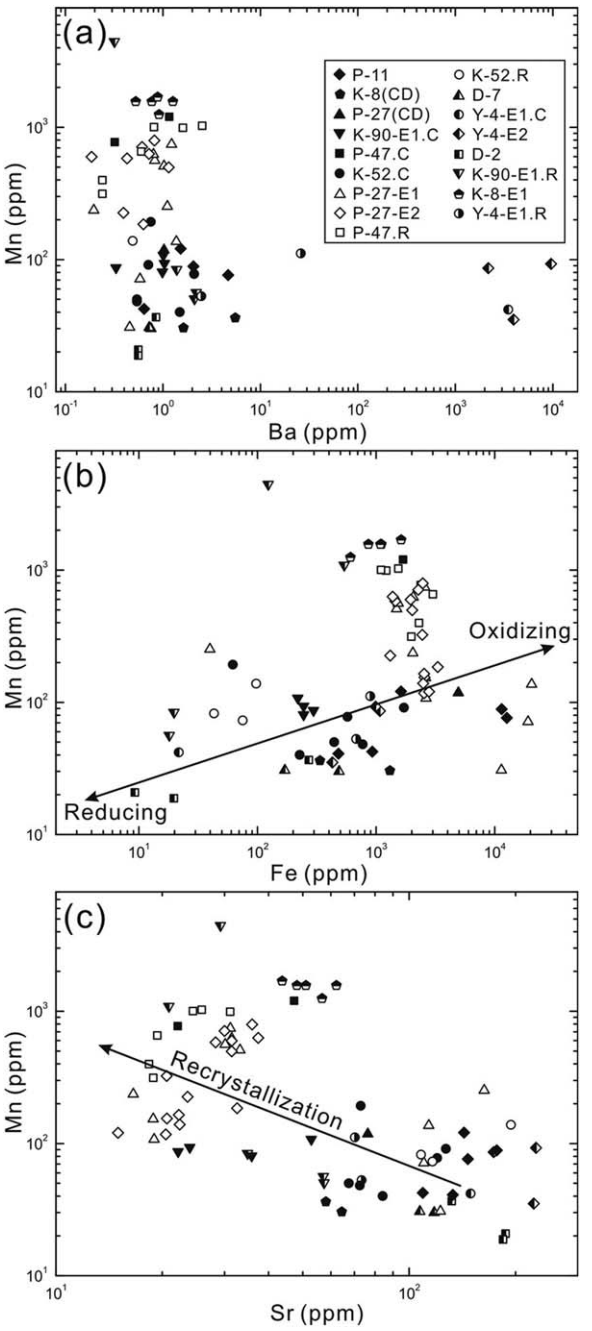

Figure 11. Binary diagrams of (a) Ba, (b) Fe, and (c) Sr versus Mn for estimating characteristics of diagenetic fluids. Ba versus Mn can reflect participation of hydrothermal fluids. Fe versus Mn can indicate redox environment of dolomite formation. Sr versus Mn can recognize recrystallization of dolomites during diagenesis. Solid symbol, dolomites with T1 patterns; open symbol, dolomites with T2 patterns; half left symbol, dolomites with T3 patterns; half up symbol, dolomites with T4 patterns; half right symbol, dolomites with T5 patterns. CD, dolomite grains in crystalline dolomites; C, core; R, rim. For data see supporting information Table S3.

We suggest that the related diagenetic fluids were likely to be derived from deep-circulating meteoric or marine water carrying crustal features from Cambrian and Precambrian evaporites and detrital rocks [*Li et al*., 2011] without involvement of magmatic hydrothermal fluids. Note that the outer rims of Samples P-27-E1 and P-27-E2 (Figure 7) display obvious Eu anomalies (Figure 6b) and relatively low contents of Fe and Mn (Figure 11b), implying the probable influence of magmatic hydrothermal fluids (for detailed interpretation, see next section).

5.4.3. Dolomite With T3 and T4 REE Pattern

Most of dolomite samples with T3 and T4 REE patterns (e.g., Samples Y-4-E1 and K-8-E1) have relatively high Ba or Mn contents, indicating the derivation of hydrothermal fluids (Figure 11a). Studies on the fluid inclusions in this kind of diagenetic dolomites from the Tarim basin demonstrated that the homogenization temperatures could reach 173–200°C [*Zhu et al*., 2010; *Zhao et al*., 2012]. Furthermore, most of these dolomite samples show relatively high Sr and low Mn contents (Figure 11c), which indicates they were precipitated from the diagenetic fluids directly instead of recrystallization (recrystallization would result in depletion of Sr and enrichment of Mn) from host rocks [*Qing*, 1998; *Hecht et al*., 1999; *Jacobsen and Kaufman*, 1999; *Derry*, 2010]. This can also be proved by clearer dolomite crystals with big size and bright red or even orange yellow CL (Table 1), as well as MgO-Mg/Ca diagram (Figure 5), where these diagenetic dolomite samples fall near the theoretical composition of stoichiometric dolomite [*Warren*, 2000; *Chen et al*., 2010]. There is a little difference between T3 and T4 patterns. Relatively flat REEs and low ΣREE values are shown in T3 patterns, while obvious LREE enrichment and high ΣREE are shown in T4 patterns (Figures 9d and 9e). This may be related to the occurrence of associated quartz veins in dolomite samples with T4 patterns (Sample K-8-E1; Figure 4h), and the further study is need to provide the accurate interpretation.

It is notable that these dolomites show significantly positive Eu anomalies (Figures 6b, 9d, and 9e). Positive Eu anomalies of hydrothermal fluids can be inherited by fluid-rock interaction with feldspars [*McLennan*, 1989] but physicochemical conditions are also important [*Bau*, 1991; *Hecht et al*., 1999]. In high-temperature regimes

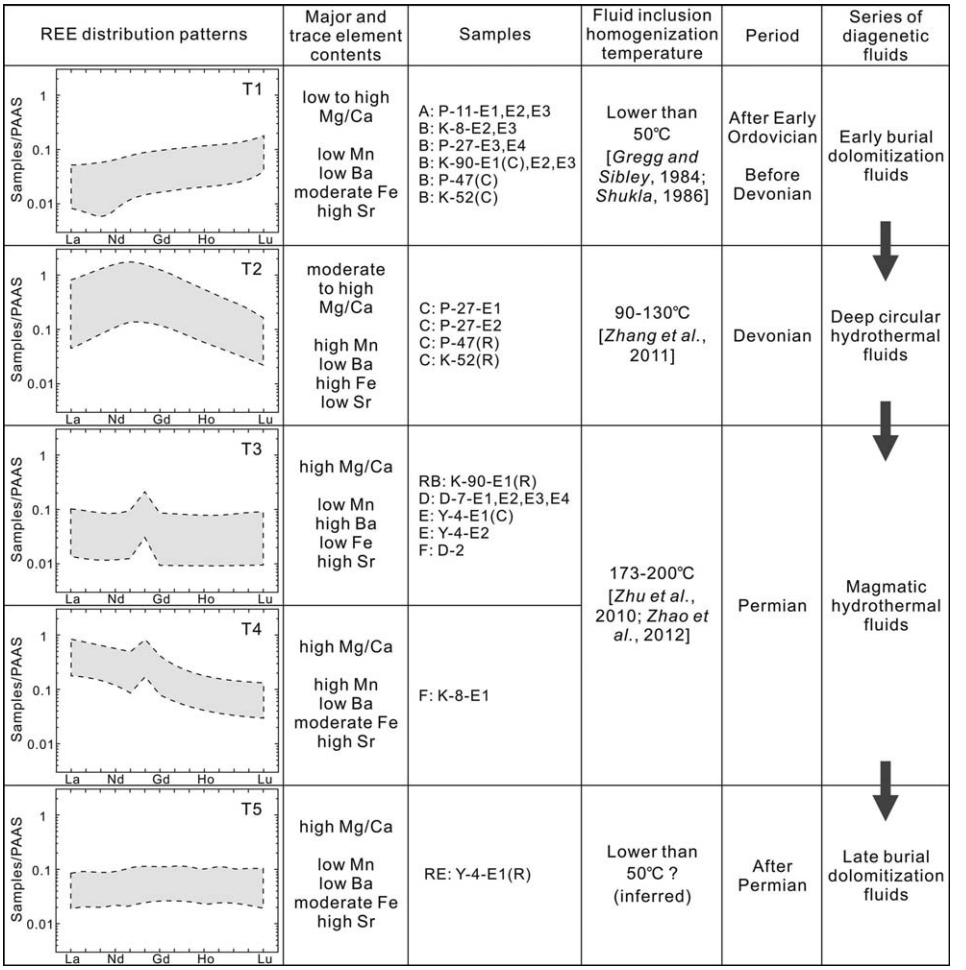

Figure 12. A summary of major, trace, and rare earth elements of the analyzed dolomites and the nature and origin of the related diagenetic fluids. The data of fluid inclusion homogenization temperatures are from references. A–F represent dolomite types based on the petrology examination (for details see the text); RB, rim of dolomite grain in crystalline dolomites; RE, rim of dolomite grain in siliceous rocks; (C), core; (R), rim. T1–T5 represent dolomite types divided by geochemical features in Figure 9.

(>200–250°C), Eu^{2+} can be fractionated from the other REE because with increasing temperature, the oxygen fugacity at which Eu^{3+} is reduced to Eu^{2+} increases and the reduction occurs more easily [*Bau and Möller*, 1992; *Bau and Dulski*, 1996; *Hecht et al*., 1999]. Besides, the larger water/rock ratio (w/r) is, the lower temperature for reduction is required [*Bau*, 1991]. The REE pattern of the fluid is considered to be controlled by sorption processes under acidic conditions, which preferentially provided Eu as Eu^{2+} status and thus results in positive Eu anomaly in the fluid [*Bau*, 1991; *Kučera et al*., 2009; *Morgan et al*., 2013]. Therefore, positive Eu anomalies are typically found in acidic, reducing hydrothermal fluids [*Frimmel*, 2009]. The reducing environment is also indicated by relatively low contents of Fe and Mn (Figure 11b) and slightly positive Ce anomalies (Figure 6c) in dolomite samples with T3 and T4 REE patterns because Ce depletion absents in hydrothermal precipitates as a result of a shift of the Ce^{4+}/Ce^{3+} redox equilibrium toward higher oxygen fugacity with increasing temperature [*Frimmel*, 2009].

We infer that these acidic, reducing, and extremely high-temperature (~200°C) diagenetic fluids were most likely to be derived from the magmatic hydrothermal fluids. Note that Samples D-2 and D-7 were collected from an outcrop section (i.e., DBTG Section) where a 3 m thick diabase sill intruded roughly along the strata (Figure 3a). Permian volcanic-magmatic events were highly active in the Tarim basin [*Yang et al*., 2007; *C. L. Zhang et al*., 2008; *Zhang et al*., 2010; *Zhou et al*., 2009; *Tian et al*., 2010; *Yu et al*., 2011]. Also, both acidic and basic magmatic eruptions and diabase intrusions were widely found in the northwestern Tarim basin [*Yang et al*., 2007; *Zhang et al*., 2010; *Tian et al*., 2010], which could provide the acidic, reducing, hydrothermal

diagenetic fluids with high w/r, and thus strongly influence the underlying dolomite strata. Furthermore, the Precambrian basement of the basin contains plenty of magmatic rocks including granite, bimodal volcanic rocks, and mafic dike swarms [*Wang et al*., 2010; *Zhai*, 2013] and siliciclastic rocks [*Li et al*., 2011; *Zhai*, 2013], which are rich in Eu-bearing plagioclase. The magmatic hydrothermal fluids which interacted with these plagioclase-rich rocks during the migration upward can be rich in Eu and easily generate positive Eu anomalies for the diagenetic dolomites [*Kučera et al*., 2009]. This can also be supported by integrated isotopic geochemistry (C, O, and Sr) and fluid inclusion microthermometry [*Dong et al*., 2013a], which suggest that dolomite precipitation were associated with the hydrothermal activities induced by intrusive magmatism.

5.4.4. Dolomite With T5 REE Pattern

Dolomite with T5 REE patterns (e.g., rim of Sample Y-4-E1) has similar geochemical features with the ones with T1 REE patterns. Thus, it was also probably formed from weakly oxidizing connate brines during burial. However, petrographic observation indicates that this kind dolomite was generated after dolomites with T1 REE patterns. Therefore, we consider that dolomite with T5 REE patterns was derived from burial dolomitizing fluids as well, but probably in later diagenetic stages.

5.5. Potential Evolution of the Diagenetic Fluids for the Dolomites

As mentioned in the preceding discussion, dolomite samples with T3 and T4 patterns were likely formed during the Late Hercynian, related to Permian volcanic-magmatic events. *Dong et al*. [2013a] also determined that the timing of hydrothermal dolomitization was constrained within the Early Permian based on the basin analysis (e.g., regional tectonic history). Since the outer rims of Samples P-27-E1 and P-27-E2 (Figure 7) were probably influenced by the magmatic hydrothermal fluids, we infer that deep-circulating crustal hydrothermal fluids (linked to dolomites with T2 patterns) should be earlier than Permian magmatic hydrothermal fluids and controlled by primary regional tectonic events and related faults. *Tang et al*. [2012] summarized controls on the formation and evolution of the fault structures in the Tarim basin could be divided into seven tectonic stages, i.e., Early Caledonian, Middle Caledonian, Late Caledonian-Early Hercynian, Late Hercynian, Indosinian, Yanshanian, and Himalayan, thus the deep-circulating crustal hydrothermal fluids were most likely formed during the Late Caledonian-Early Hercynian (i.e., Devonian), when a great number of thrust faults were produced in the northwestern Tarim basin [*Tang et al*., 2012]. This deduction can also be supported by burial-thermal history reported by *Ye* [1994] and *Li et al*. [2011].

Therefore, the potential diagenetic fluid evolution can be described as follows (as summarized in Figure 12): (1) low-temperature burial dolomitizing fluids under weak oxidation conditions in the early diagenetic stage; (2) relatively low-temperature deep-circulating crustal hydrothermal fluids under suboxic conditions during the Devonian; (3) acidic, reducing, magmatic hydrothermal fluids related to Permian volcanic activity; and (4) burial dolomitizing fluids in later diagenetic stages.

Consequently, on the basis of *in situ* geochemical analysis and supported by petrographic observation, our study unravels the debatable issue concerning the nature, origin, and evolution of the diagenetic fluids for Lower Paleozoic dolomites in the northwestern Tarim basin. Taking saddle dolomites filling in the vugs, for example, we infer they are probably associated with the deep-circulating crustal hydrothermal fluids, which supports the views of *Zhang et al*. [2009] and *Pan et al*. [2012].

6. Conclusions

This study combines petrography, *in situ* major, trace, and rare earth element geochemistry of Lower Paleozoic diagenetic dolomites in carbonate rocks and siliceous rocks in the northwestern Tarim basin and yields the following conclusion concerning geochemical features and origin of the dolomites and related diagenetic fluids.

Six types of diagenetic dolomites can be distinguished based on petrographic observation, including (A) dolomite grains in limestones; (B) dolomite grains in crystalline dolomites; (C) saddle dolomites filling in vugs; (D) dolomite cements in calcarenites; (E) dolomite grains in siliceous rocks; and (F) dolomite veins in siliceous rocks.

By focusing on individual spots within dolomite crystals, the *in situ* analysis results demonstrate that the geochemical data are not influenced by contamination from other components of the samples; thus, this method is preferred compared with the whole rock analysis. The geochemical features of the diagenetic dolomites can be divided into five types, and each type is probably formed (or controlled) by specific

diagenetic fluid as follows. (T1) HREE enrichment, low ΣREE, no Eu anomaly, low to high Mg/Ca ratios, low Mn and Ba, moderate Fe, and high Sr contents, the dolomites could be related to low-temperature burial dolomitization under weakly oxidizing conditions during early diagenesis; (T2) MREE enrichment, high ΣREE, various Eu anomalies, moderate to high Mg/Ca ratios, high Mn, Fe, and low Ba, Sr contents, the dolomites were probably the result of recrystallization controlled by relatively low-temperature crustal hydrothermal fluids under suboxic conditions; (T3) flat REE pattern, moderate ΣREE, positive Eu anomaly, high Mg/Ca ratios, high Ba, Sr, and low Mn, Fe contents; (T4) LREE enrichment, high ΣREE, positive Eu anomaly, high Mg/Ca ratios, high Mn and Sr, moderate Fe, and low Ba contents, the dolomites with these two patterns were likely to be directly precipitated from acidic, reducing, magmatic hydrothermal fluids; (T5) flat REE pattern, moderate ΣREE, no Eu anomaly, high Mg/Ca ratios, low Mn and Ba, moderate Fe, and high Sr contents, the dolomites could be associated with the burial dolomitizing fluids in later diagenetic stages.

According to the dolomite small-scale geochemical variations obtained by *in situ* method as well as the petrographic features, the debated issue about the nature and evolution of diagenetic fluids has been solved. Four stages of the evolution of diagenetic fluids for Lower Paleozoic dolomites can be inferred (in order): (1) early burial dolomitizing fluids; (2) Devonian deep-circulating hydrothermal fluids; (3) Permian magmatic hydrothermal fluids; and (4) late burial dolomitizing fluids. The data of this study also reveal that *in situ* method, rather than whole rock analysis, should be preferentially applied in geochemical studies of complicated diagenetic history.

Acknowledgments

This work is supported by the (973) National Basic Research Program of China (Grant 2012CB214801), the Major National S&T Program of China (Grant 2011ZX05009-002-403 and 2011ZX05004-004-005), and the grants from PetroChina Tarim Oilfield Company. We appreciate R. Liu and Y. Jin for their assistance in sampling, Z. Chen, J. Du, and F. Ma for their help in laboratory analysis, and Y. Li for her critically suggestions of the manuscript. We also thank the Editor Louis A. Derry and two anonymous reviewers for their detailed and constructive comments, which led to a better presentation of the manuscript.

References

Alexander, B. W., M. Bau, P. Andersson, and P. Dulski (2008), Continentally-derived solutes in shallow Archean seawater: Rare earth element and Nd isotope evidence in iron formation from the 2.9 Ga Pongola Supergroup, South Africa, *Geochim. Cosmochim. Acta*, *72*(2), 378–394, doi:10.1016/j.gca.2007.10.028.

Alibo, D. S., and Y. Nozaki (1999), Rare earth elements in seawater: Particle association, shalenormalization, and Ce oxidation, *Geochim. Cosmochim. Acta*, *63*(3–4), 363–372, doi:10.1016/S0016-7037(98)00279-8.

Azomani, E., K. Azmy, N. Blamey, U. Brand, and I. Al-Aasm (2013), Origin of Lower Ordovician dolomites in eastern Laurentia: Controls on porosity and implications from geochemistry, *Mar. Pet. Geol.*, *40*, 99–114, doi:10.1016/j.marpetgeo.2012.10.007.

Baldwin, G. J., P. C. Thurston, and B. S. Kamber (2011), High-precision rare earth element, nickel, and chromium chemistry of chert microbands pre-screened with in-situ analysis, *Chem. Geol.*, *285*(1–4), 133–143, doi:10.1016/j.chemgeo.2011.03.019.

Banner, J. L., G. N. Hanson, and W. J. Meyers (1988), Rare earth element and Nd isotopic variations in regionally extensive dolomites from the Burlington-Keokuk Formation (Mississippian): Implications for REE mobility during carbonate diagenesis, *J. Sediment. Res.*, *58*(3), 415–432, doi:10.1306/212F8DAA-2B24-11D7-8648000102C1865D.

Bau, M. (1991), Rare-earth element mobility during hydrothermal and metamorphic fluid-rock interaction and the significance of the oxidation state of europium, *Chem. Geol.*, *93*(3–4), 219–230, doi:10.1016/0009-2541(91)90115-8.

Bau, M., and P. Dulski (1996), Distribution of yttrium and rare-earth elements in the Penge and Kuruman iron-formations, Transvaal Supergroup, South Africa, *Precambrian Res.*, *79*(1–2), 37–55, doi:10.1016/0301-9268(95)00087-9.

Bau, M., and P. Möller (1992), Rare earth element fractionation in metamorphogenic hydrothermal calcite, magnesite and siderite, *Mineral. Petrol.*, *45*(3–4), 231–246, doi:10.1007/BF01163114.

Bau, M., A. Koschinsky, P. Dulski, and J. R. Hein (1996), Comparison of the partitioning behaviours of yttrium, rare earth elements, and titanium between hydrogenetic marine ferromanganese crusts and seawater, *Geochim. Cosmochim. Acta*, *60*(10), 1709–1725, doi:10.1016/0016-7037(96)00063-4.

Bolhar, R., and M. J. Van Kranendonk (2007), A non-marine depositional setting for the northern Fortescue Group, Pilbara Craton, inferred from trace element geochemistry of stromatolitic carbonates, *Precambrian Res.*, *155*(3–4), 229–250, doi:10.1016/j.precamres.2007.02.002.

Bolhar, R., B. S. Kamber, S. Moorbath, C. M. Fedo, and M. J. Whitehouse (2004), Characterisation of early Archaean chemical sediments by trace element signatures, *Earth Planet. Sci. Lett.*, *222*(1), 43–60, doi:10.1016/j.epsl.2004.02.016.

Bristow, T. F., M. Bonifacie, A. Derkowski, J. M. Eiler, and J. P. Grotzinger (2011), A hydrothermal origin for isotopically anomalous cap dolostone cements from south China, *Nature*, *474*(7349), 68–71, doi:10.1038/nature10096.

Cai, C., W. Hu, and R. H. Worden (2001a), Thermochemical sulphate reduction in Cambro–Ordovician carbonates in Central Tarim, *Mar. Pet. Geol.*, *18*(6), 729–741, doi:10.1016/S0264-8172(01)00028-9.

Cai, C., S. G. Franks, and P. Aagaard (2001b), Origin and migration of brines from Paleozoic strata in Central Tarim, China: Constraints from $^{87}Sr/^{86}Sr$, δD, $\delta^{18}O$ and water chemistry, *Appl. Geochem.*, *16*(9–10), 1269–1284, doi:10.1016/S0883-2927(01)00006-3.

Cai, C., K. Li, H. Li, and B. Zhang (2008), Evidence for cross formational hot brine flow from integrated $^{87}Sr/^{86}Sr$, REE and fluid inclusions of the Ordovician veins in Central Tarim, China, *Appl. Geochem.*, *23*(8), 2226–2235, doi:10.1016/j.apgeochem.2008.03.009.

Chen, L., Y. Liu, Z. Hu, S. Gao, K. Zong, and H. Chen (2011), Accurate determinations of fifty-four major and trace elements in carbonate by LA–ICP-MS using normalization strategy of bulk components as 100%, *Chem. Geol.*, *284*(3), 283–295, doi:10.1016/j.chemgeo.2011.03.007.

Chen, Y., X. Zhou, K. Zhao, W. Yang, and C. Dong (2009), The petrologic rhythm of Lower Ordovician Penglaiba Formation encountered by Well Tazhong 19 and new dolomitization model, Tarim basin [in Chinese with English abstract], *Acta Sedimentol. Sin.*, *27*(2), 202–210.

Chen, Y., X. Zhou, and H. Yang (2010), Geochemical research and genesis of dolostones with different crystal characteristics occurring in the Upper Cambrian, central area of Tarim basin [in Chinese with English abstract], *Acta Sedimentol. Sin.*, *28*(2), 209–218.

Derry, L. A. (2010), A burial diagenesis origin for the Ediacaran Shuram-Wonoka carbon isotope anomaly, *Earth Planet. Sci. Lett.*, *294*(1), 152–162, doi:10.1016/j.epsl.2010.03.022.

Derry, L. A., and S. B. Jacobsen (1990), The chemical evolution of Precambrian seawater: Evidence from REEs in banded iron formations, *Geochim. Cosmochim. Acta*, *54*(11), 2965–2977, doi:10.1016/0016-7037(90)90114-Z.

Dong, S., D. Chen, H. Qing, X. Zhou, D. Wang, Z. Guo, M. Jiang, and Y. Qian (2013a), Hydrothermal alteration of dolostones in the Lower Ordovician, Tarim Basin, NW China: Multiple constraints from petrology, isotope geochemistry and fluid inclusion microthermometry, *Mar. Pet. Geol.*, *46*, 270–286, doi:10.1016/j.marpetgeo.2013.06.013.

Dong, S., D. Chen, H. Qing, M. Jiang, and X. Zhou (2013b), *In situ* stable isotopic constraints on dolomitizing fluids for the hydrothermally-originated saddle dolomites at Keping, Tarim Basin, *Chin. Sci. Bull.*, *58*(23), 2877–2882, doi:10.1007/s11434-013-5801-7.

Elderfield, H., R. Upstill-Goddard, and E. R. Sholkovitz (1990), The rare earth elements in rivers, estuaries, and coastal seas and their significance to the composition of ocean waters, *Geochim. Cosmochim. Acta*, *54*(4), 971–991, doi:10.1016/0016-7037(90)90432-K.

Frimmel, H. E. (2009), Trace element distribution in Neoproterozoic carbonates as palaeoenvironmental indicator, *Chem. Geol.*, *258*(3–4), 338–353, doi:10.1016/j.chemgeo.2008.10.033.

Gao, S., X. Liu, H. Yuan, B. Hattendorf, D. Günther, L. Chen, and S. Hu (2002), Determination of forty two major and trace elements in USGS and NIST SRM glasses by laser ablation-inductively coupled plasma-mass spectrometry, *Geostand. Newsl.*, *26*(2), 181–196, doi:10.1111/j.1751-908X.2002.tb00886.x.

Goldstein, S. J., and S. B. Jacobsen (1988), Rare earth elements in river waters, *Earth Planet. Sci. Lett.*, *89*(1), 35–47, doi:10.1016/0012-821X(88)90031-3.

Gregg, J. M., and D. F. Sibley (1984), Epigenetic dolomitization and the origin of xenotopic dolomite texture, *J. Sediment. Res.*, *54*(3), 908–931, doi:10.1306/212F8535-2B24-11D7-8648000102C1865D.

Han, Y. X., Z. Li, D. L. Han, S. T. Peng, and J. Q. Liu (2009), REE characteristics of matrix dolomites and its origin of Lower Ordovician in eastern Tabei area, Tarim basin [in Chinese with English abstract], *Acta Petrol. Sin.*, *25*(10), 2405–2416.

Hecht, L., R. Freiberger, H. A. Gilg, G. Grundmann, and Y. A. Kostitsyn (1999), Rare earth element and isotope (C, O, Sr) characteristics of hydrothermal carbonates: Genetic implications for dolomite-hosted talc mineralization at Göpfersgrün (Fichtelgebirge, Germany), *Chem. Geol.*, *155*(1–2), 115–130, doi:10.1016/S0009-2541(98)00144-2.

Hu, W., Q. Chen, X. Wang, and J. Cao (2010), REE models for the discrimination of fluids in the formation and evolution of dolomite reservoirs [in Chinese with English abstract], *Oil Gas Geol.*, *31*(6), 810–818.

Jacobsen, S. B., and A. J. Kaufman (1999), The Sr, C and O isotopic evolution of Neoproterozoic seawater, *Chem. Geol.*, *161*(1–3), 37–57, doi:10.1016/S0009-2541(99)00080-7.

Ji, C., H. Qing, D. Chen, P. Luo, Z. Jin, and L. Shao (2013), Characteristics and dolomitization of Upper Cambrian to Lower Ordovician dolomite from outcrop in Keping Uplift, Western Tarim Basin, Northwest China, *Acta Geol. Sin.*, *87*(4), 1005–1018, doi:10.1111/1755-6724.12106.

Jian, X., P. Guan, D. W. Zhang, W. Zhang, F. Feng, R. J. Liu, and S. D. Lin (2013a), Provenance of Tertiary sandstone in the northern Qaidam basin, northeastern Tibetan Plateau: Integration of framework petrography, heavy mineral analysis and mineral chemistry, *Sediment. Geol.*, *290*, 109–125, doi:10.1016/j.sedgeo.2013.03.010.

Jian, X., P. Guan, W. Zhang, and F. Feng (2013b), Geochemistry of Mesozoic and Cenozoic sediments in the northern Qaidam basin, northeastern Tibetan Plateau: Implications for provenance and weathering, *Chem. Geol.*, *360–361*, 74–88, doi:10.1016/j.chemgeo.2013.10.011.

Jiao, C. L., Z. L. He, X. J. Xing, H. R. Qing, B. Z. He, and C. C. Li (2011), Tectonic hydrothermal dolomite and its significance of reservoirs in Tarim basin [in Chinese with English abstract], *Acta Petrol. Sin.*, *27*(1), 277–284.

Jin, Z., D. Zhu, W. Hu, X. Zhang, Y. Wang, and X. Yan (2006), Geological and geochemical signatures of hydrothermal activity and their influence on carbonate reservoir beds in the Tarim basin [in Chinese with English abstract], *Acta Geol. Sin.*, *80*(2), 245–253.

Jochum, K. P., D. Scholz, B. Stoll, U. Weis, S. A. Wilson, Q. Yang, A. Schwalb, N. Börner, D. E. Jacob, and M. O. Andreae (2012), Accurate trace element analysis of speleothems and biogenic calcium carbonates by LA-ICP-MS, *Chem. Geol.*, *318–319*, 31–44, doi:10.1016/j.chemgeo.2012.05.009.

Kamber, B. S., and G. E. Webb (2001), The geochemistry of late Archaean microbial carbonate: Implications for ocean chemistry and continental erosion history, *Geochim. Cosmochim. Acta*, *65*(15), 2509–2525, doi:10.1016/S0016-7037(01)00613-5.

Kamber, B. S., and G. E. Webb (2007), Transition metal abundances in microbial carbonate: A pilot study based on *in situ* LA-ICP-MS analysis, *Geobiology*, *5*(4), 375–389, doi:10.1111/j.1472-4669.2007.00129.x.

Katz, D. A., G. P. Eberli, P. K. Swart, and L. B. Smith Jr. (2006), Tectonic-hydrothermal brecciation associated with calcite precipitation and permeability destruction in Mississippian carbonate reservoirs, Montana and Wyoming, *AAPG Bull.*, *90*(11), 1803–1841, doi:10.1306/03200605072.

Kučera, J., J. Cempírek, Z. Dolníček, P. Muchez, and W. Prochaska (2009), Rare earth elements and yttrium geochemistry of dolomite from post-Variscan vein-type mineralization of the Nízký Jeseník and Upper Silesian Basins, Czech Republic, *J. Geochem. Explor.*, *103*(2–3), 69–79, doi:10.1016/j.gexplo.2009.08.001.

Lapponi, F., T. Bechstädt, M. Boni, D. A. Banks, and J. Schneider (2013), Hydrothermal dolomitization in a complex geodynamic setting (Lower Palaeozoic, northern Spain), *Sedimentology*, *61*(2), 411–443, doi:10.1111/sed.12060.

Lazartigues, A. V., P. Sirois, and D. Savard (2014), LA-ICP-MS analysis of small samples: Carbonate reference materials and larval fish otoliths, *Geostand. Geoanal. Res.*, doi:10.1111/j.1751-908X.2013.00248.x, in press.

Li, H., N. Qiu, Z. Jin, and Z. He (2005), Geothermal history of Tarim basin [in Chinese with English abstract], *Oil Gas Geol.*, *26*(5), 613–617.

Li, K., C. Cai, H. He, L. Jiang, L. Cai, L. Xiang, S. Huang, and C. Zhang (2011), Origin of palaeo-waters in the Ordovician carbonates in Tahe oilfield, Tarim Basin: Constraints from fluid inclusions and Sr, C and O isotopes, *Geofluids*, *11*(1), 71–86, doi:10.1111/j.1468-8123.2010.00312.x.

Li, X. W., X. X. Mo, X. H. Yu, Y. Ding, X. F. Huang, P. Wei, and W. Y. He (2013), Petrology and geochemistry of the early Mesozoic pyroxene andesites in the Maixiu Area, West Qinling, China: Products of subduction or syn-collision? *Lithos*, *172–173*, 158–174, doi:10.1016/j.lithos.2013.04.010.

Lonnee, J., and H. G. Machel (2006), Pervasive dolomitization with subsequent hydrothermal alteration in the Clarke Lake gas field, Middle Devonian Slave Point Formation, British Columbia, Canada, *AAPG Bull.*, *90*(11), 1739–1761, doi:10.1306/03060605069.

Lu, S., H. Li, C. Zhang, and G. Niu (2008), Geological and geochronological evidence for the Precambrian evolution of the Tarim Craton and surrounding continental fragments, *Precambrian Res.*, *160*(1), 94–107, doi:10.1016/j.precamres.2007.04.025.

Lüders, V., P. Möller, and P. Dulski (1993), REE fractionation in carbonates and fluorites, *Monogr. Ser. Mineral Deposits*, *30*(9), 133–150.

McLennan, S. (1989), Rare earth elements in sedimentary rocks: Influence of provenance and sedimentary processes, *Rev. Mineral. Geochem.*, *21*(1), 169–200.

Middleton, K., M. Coniglio, R. Sherlock, and S. K. Frape (1993), Dolomitization of Middle Ordovician carbonate reservoirs, southwestern Ontario, *Bull. Can. Pet. Geol.*, *41*(2), 150–163.

Morford, J. L., and S. Emerson (1999), The geochemistry of redox sensitive trace metals in sediments, *Geochim. Cosmochim. Acta*, *63*(11–12), 1735–1750, doi:10.1016/S0016-7037(99)00126-X.

Morgan, J. W., and G. A. Wandless (1980), Rare earth elements in some hydrothermal minerals: Evidence of crystallographic control, *Geochim. Cosmochim. Acta*, *44*(7), 973–980, doi:10.1016/0016-7037(80)90286-0.

Morgan, R., B. Orberger, C. A. Rosière, R. Wirth, C. M. Carvalho, and M. T. Bellver-Baca (2013), The origin of coexisting carbonates in banded iron formations: A micro-mineralogical study of the 2.4 Ga Itabira Group, Brazil, *Precambrian Res.*, *224*, 491–511, doi:10.1016/j.precamres.2012.10.013.

Nothdurft, L. D., G. E. Webb, and B. S. Kamber (2004), Rare earth element geochemistry of Late Devonian reefal carbonates, Canning Basin, Western Australia: Confirmation of a seawater REE proxy in ancient limestones, *Geochim. Cosmochim. Acta*, *68*(2), 263–283, doi:10.1016/S0016-7037(03)00422-8.

Pan, W., Y. Liu, J. A. D. Dickson, A. Shen, J. Han, Y. Ye, H. Gao, P. Guan, L. Zhang, and X. Zheng (2009), The geological model of hydrothermal activity in outcrop and the characteristics of carbonate hydrothermal karst of Lower Paleozoic in Tarim basin [in Chinese with English abstract], *Acta Sedimentol. Sin.*, *27*(5), 983–994.

Pan, W. Q., X. F. Hu, Y. L. Liu, Q. D. Gao, and Y. Ye (2012), Geological and geochemical evidences for two sources of hydrothermal fluids found in Ordovician carbonate rocks in northwestern Tarim Basin [in Chinese with English abstract], *Acta Pet. Sin.*, *28*(8), 2515–2524.

Piqué, À., À. Canals, F. Grandia, and D. A. Banks (2008), Mesozoic fluorite veins in NE Spain record regional base metal-rich brine circulation through basin and basement during extensional events, *Chem. Geol.*, *257*(1–2), 139–152, doi:10.1016/j.chemgeo.2008.08.028.

Qian, Y. X., D. H. You, D. Z. Chen, H. R. Qing, Z. L. He, Y. C. Ma, M. Tian, and B. B. Xi (2012), The petrographic and geochemical signatures and implication of origin of the Middle and Upper Cambrian dolostone in eastern margin Tarim: Comparative studies with the Whirlpool point of the Western Canada Sedimentary Basin [in Chinese with English abstract], *Acta Petrol. Sin.*, *28*(8), 2525–2541.

Qing, H. (1998), Petrography and geochemistry of early-stage, fine- and medium-crystalline dolomites in the Middle Devonian Presqu'ile Barrier at Pine Point, Canada, *Sedimentology*, *45*(2), 433–446, doi:10.1046/j.1365-3091.1998.0154f.x.

Qing, H., and E. W. Mountjoy (1994), Rare earth element geochemistry of dolomites in the Middle Devonian Presqu'ile barrier, Western Canada Sedimentary Basin: Implications for fluid-rock ratios during dolomitization, *Sedimentology*, *41*(4), 787–804, doi:10.1111/j.1365-3091.1994.tb01424.x.

Schwinn, G., and G. Markl (2005), REE systematics in hydrothermal fluorite, *Chem. Geol.*, *216*(3–4), 225–248, doi:10.1016/j.chemgeo.2004.11.012.

Shao, L., J. Han, F. Ma, Y. Liu, H. Xu, G. Wu, and C. Ji (2010), Characteristics of the Cambrian dolomite reservoirs and their facies-controlling in eastern Tarim basin [in Chinese with English abstract], *Acta Sedimentol. Sin.*, *28*(5), 953–961.

Shields, G. A., and G. E. Webb (2004), Has the REE composition of seawater changed over geological time?, *Chem. Geol.*, *204*(1–2), 103–107, doi:10.1016/j.chemgeo.2003.09.010.

Shukla, V., J. M. Gregg, and D. F. Sibley (1986), Epigenetic dolomitization and origin of xenotopic dolomite texture: Discussion and reply, *J. Sediment. Petrol.*, *56*(5), 733–736.

Sinclair, D. J., L. P. Kinsley, and M. T. McCulloch (1998), High resolution analysis of trace elements in corals by laser ablation ICP-MS, *Geochim. Cosmochim. Acta*, *62*(11), 1889–1901, doi:10.1016/S0016-7037(98)00112-4.

Tang, L. (1997), Major evolutionary stages of Tarim Basin in Phanerozoic Time [in Chinese with English abstract], *Earth Sci. Front.*, *4*(3–4), 318–324.

Tang, L. J., L. X. Qi, H. J. Qiu, L. Yun, M. Li, D. Q. Xie, Y. Yang, and G. M. Wan (2012), Poly-phase differential fault movement and hydrocarbon accumulation of the Tarim Basin, NW China [in Chinese with English abstract], *Acta Petrol. Sin.*, *28*(8), 2569–2583.

Taylor, S. R., and S. M. McLennan (1985), The Continental Crust: Its Composition and Evolution, 312 pp., Blackwell Sci., Malden, Mass.

Tian, W., I. H. Campbell, C. M. Allen, P. Guan, W. Pan, M. Chen, H. Yu, and W. Zhu (2010), The Tarim picrite–basalt–rhyolite suite, a Permian flood basalt from northwest China with contrasting rhyolites produced by fractional crystallization and anatexis, *Contrib. Mineral Petrol.*, *160*(3), 407–425, doi:10.1007/s00410-009-0485-3.

Tlig, S., and A. M'Rabet (1985), A comparative study of the rare earth element (REE) distributions within the Lower Cretaceous dolomites and limestones of Central Tunisia, *Sedimentology*, *32*(6), 897–907, doi:10.1111/j.1365-3091.1985.tb00739.x.

Tuo, J., and R. P. Philp (2003), Occurrence and distribution of high molecular weight hydrocarbons in selected non-marine source rocks from the Liaohe, Qaidam and Tarim Basins, China, *Org. Geochem.*, *34*(11), 1543–1558, doi:10.1016/S0146-6380(03)00174-8.

Wang, F., B. Wang, and L. S. Shu (2010), Continental tholeiitic basalt of the Akesu area (NW China) and its implication for the Neoproterozoic rifting in the northern Tarim [in Chinese with English abstract], *Acta Petrol. Sin.*, *26*(2), 547–558.

Wang, Q. M., T. Nishidai, and M. P. Coward (1992), The Tarim Basin, NW China: Formation and aspects of petroleum geology, *J. Pet. Geol.*, *15*(1), 5–34, doi:10.1111/j.1747-5457.1992.tb00863.x.

Wang, X., Z. Jin, W. Hu, J. Zhang, Y. Qian, J. Zhu, and Q. Li (2009), Using *in situ* REE analysis to study the origin and diagenesis of dolomite of Lower Paleozoic, Tarim Basin, *Sci. China Ser. D*, *52*(5), 681–693, doi:10.1007/s11430-009-0057-4.

Warren, J. (2000), Dolomite: Occurrence, evolution and economically important associations, *Earth Sci. Rev.*, *52*(1–3), 1–81, doi:10.1016/S0012-8252(00)00022-2.

Webb, G. E., and B. S. Kamber (2000), Rare earth elements in Holocene reefal microbialites: A new shallow seawater proxy, *Geochim. Cosmochim. Acta*, *64*(9), 1557–1565, doi:10.1016/S0016-7037(99)00400-7.

Xing, F. C., W. H. Zhang, and S. T. Li (2011), Influence of hot fluids on reservoir property of deep buried dolomite strata and its significance for petroleum exploration: A case study of Keping outcrop in Tarim basin [in Chinese with English abstract], *Acta Petrol. Sin.*, *27*(1), 266–276.

Xu, Z. Q., S. T. Li, J. X. Zhang, J. S. Yang, B. Z. He, H. B. Li, C. S. Lin, and Z. H. Cai (2011), Paleo-Asian and Tethyan tectonic systems with docking the Tarim block [in Chinese with English abstract], *Acta Petrol. Sin.*, *27*(1), 1–22.

Yang, S. F., Z. Li, H. Chen, M. Santosh, C. W. Dong, and X. Yu (2007), Permian bimodal dyke of Tarim Basin, NW China: Geochemical characteristics and tectonic implications, *Gondwana Res.*, *12*(1–2), 113–120, doi:10.1016/j.gr.2006.10.018.

Ye, D. (1994), Deep dissolution of Cambrian-Ordovician carbonates in the Northern Tarim Basin [in Chinese with English abstract], *Acta Sedimentol. Sin.*, *12*(1), 66–71.

Yu, X., S. F. Yang, H. L. Chen, Z. Q. Chen, Z. L. Li, G. E. Batt, and Y. Q. Li (2011), Permian flood basalts from the Tarim Basin, Northwest China: SHRIMP zircon U-Pb dating and geochemical characteristics, *Gondwana Res.*, *20*(2), 485–497, doi:10.1016/j.gr.2010.11.009.

Zhai, M. (2013), The main old lands in China and assembly of Chinese unified continent, *Sci. China Ser. D*, *56*(11), 1829–1852, doi:10.1007/s11430-013-4665-7.

Zhang, C., D. Zheng, and J. Li (2001), Attribute of paleozoic structures and its evolution characteristics in Keping Fauit-Uplift [in Chinese with English abstract], *Oil Gas Geol.*, *22*(4), 314–318.

Zhang, C. L., X. H. Li, Z. X. Li, H. M. Ye, and C. N. Li (2008), A Permian layered intrusive complex in the western Tarim block, northwestern China: Product of a Ca. 275 Ma mantle plume, *J. Geol.*, *116*(3), 269–287, doi:10.1086/587726.

Zhang, C. L., Y. G. Xu, Z. X. Li, H. Y. Wang, and H. M. Ye (2010), Diverse Permian magmatism in the Tarim Block, NW China: Genetically linked to the Permian Tarim mantle plume?, *Lithos*, *119*(3–4), 537–552, doi:10.1016/j.lithos.2010.08.007.

Zhang, J., W. Hu, Y. Qian, X. Wang, J. Zhu, H. Zhang, J. Su, and S. Wu (2008), Feature and origin of dolomite filling in the Upper Cambrian-Lower Ordovician dolostone of the central uplift, Tarim basin [in Chinese with English abstract], *Acta Sedimentol. Sin.*, *26*(6), 957–966.

Zhang, J., W. Hu, Y. Qian, X. Wang, J. Cao, J. Zhu, Q. Li, and X. Xie (2009), Formation of saddle dolomites in Upper Cambrian carbonates, western Tarim Basin (northwest China): Implications for fault-related fluid flow, *Mar. Pet. Geol.*, *26*(8), 1428–1440, doi:10.1016/j.marpetgeo.2009.04.004.

Zhang, J., W. Hu, X. Wang, Y. Qian, and S. Wu (2011), Character and origin of Cambrian hydrothermal dolomite conglomeration in the northwestern margin of Tarim basin [in Chinese with English abstract], *Acta Geol. Sin.*, *85*(2), 234–245.

Zhang, X., W. Hu, J. Zhang, X. Wang, and X. Xie (2008a), Geochemical analyses on dolomitizing fluids of Lower Ordovician carbonate reservoir in Tarim basin [in Chinese with English abstract], *Earth Sci. Front.*, *15*(2), 80–89.

Zhang, X., W. Hu, Z. Jin, J. Zhang, Y. Qian, J. Zhu, D. Zhu, X. Wang, and X. Xie (2008b), REE compositions of Lower Ordovician dolomites in Central and North Tarim Basin, NW China: A potential REE proxy for ancient seawater, *Acta Geol. Sin.*, *82*(3), 610–621, doi:10.1111/j.1755-6724.2008.tb00611.x.

Zhao, C., B. Yu, C. Zhang, Y. Chen, and X. Qi (2012), A discussion on the formation mechanism of dolomite associated with hydrothermal solution in Tazhong area [in Chinese with English abstract], *Acta Pet. Mineral.*, *31*(2), 164–172.

Zhao, H., and B. Jones (2013), Distribution and interpretation of rare earth elements and yttrium in Cenozoic dolostones and limestones on Cayman Brac, British West Indies, *Sediment. Geol.*, *284–285*, 26–38, doi:10.1016/j.sedgeo.2012.10.009.

Zhou, M. F., J. H. Zhao, C. Y. Jiang, J. F. Gao, W. Wang, and S. H. Yang (2009), OIB-like, heterogeneous mantle sources of Permian basaltic magmatism in the western Tarim Basin, NW China: Implications for a possible Permian large igneous province, *Lithos*, *113*(3), 583–594, doi:10.1016/j.lithos.2009.06.027.

Zhu, D., Z. Jin, and W. Hu (2010), Hydrothermal recrystallization of the Lower Ordovician dolomite and its significance to reservoir in northern Tarim Basin, *Sci. China Ser. D*, *53*(3), 368–381, doi:10.1007/s11430-010-0028-9.